



# Paleoclimate Evolution on Titan After Episodic Massive Methane Outgassing Simulated by a Global Climate Model

Tetsuya Tokano<sup>1</sup>  and Ralph D. Lorenz<sup>2</sup> <sup>1</sup>Institut für Geophysik und Meteorologie, Universität zu Köln, Cologne, Germany, <sup>2</sup>Space Exploration Sector, The Johns Hopkins University Applied Physics Laboratory, Laurel, MD, USA**Key Points:**

- Massive methane outgassing into Titan's atmosphere should have caused global ice sheets if the atmosphere was previously depleted in methane
- Climate of methane snowball Titan is characterized by weak circulation, low temperature, weak seasonality and widespread snowfall
- Melting polar caps in geologically recent past may have resulted in polar seas

**Correspondence to:**T. Tokano,  
[tokano@geo.uni-koeln.de](mailto:tokano@geo.uni-koeln.de)**Citation:**

Tokano, T., & Lorenz, R. D. (2021). Paleoclimate evolution on Titan after episodic massive methane outgassing simulated by a global climate model. *Journal of Geophysical Research: Planets*, 126, e2021JE007081. <https://doi.org/10.1029/2021JE007081>

Received 30 SEP 2021

Accepted 6 DEC 2021

**Abstract** Titan's paleoclimate after the onset of the putative last major methane outgassing event 700 Myr ago is simulated by a global climate model. If the atmosphere was methane-depleted prior to outgassing, outgassed methane initially causes warming due to increased greenhouse effect. Further outgassing leads to methane snowfall, which in turn cools the troposphere and surface by an ice-albedo feedback and thereby initiates a lengthy ice age. Formation of ice sheets begins in the polar region, but with increasing methane inventory the entire globe is eventually covered by surface methane frost as thick as 100 m, with local accumulation on elevated terrains. Among various time-dependent input parameters the methane inventory by far exerts the greatest control over the climate evolution. As Titan's climate transitions from a dry state via a partially ice-covered state to a globally ice-covered state, the circulation and precipitation pattern change profoundly and the tropospheric temperature further decreases. Globally ice-covered snowball Titan is characterized by weak meridional circulation, weak seasonality and widespread snowfall. Frost ablation begins after the end of outgassing due to photochemical destruction of atmospheric methane. It is conceivable that Titan's polar seas resulted from melting of the polar caps within the past 10 Myr and subsequent drainage to the polar basins. Surface methane frost could only melt when the frost retreated to the polar region, which led to global warming by lowering of the surface albedo at low latitudes and increased greenhouse effect.

**Plain Language Summary** Saturn's moon Titan may have experienced long periods of cold climate in the past when the nitrogen atmosphere contained no methane unlike the present atmosphere. We simulated how Titan's climate may have changed when large amounts of methane were outgassed into such a cold atmosphere as indicated by models of Titan's evolution. The atmosphere can hold a certain amount of methane but the vast majority of outgassed methane condenses out as snow and is deposited on the surface. Bright methane snow on the surface keeps the surface cold and thereby prevents efficient greenhouse warming. Initially, surface methane frost is confined to high latitudes, but eventually the entire globe will be ice-covered under the assumed total amount of outgassed methane. The seasonal and global pattern of atmospheric circulation and snowfall strongly depend on the degree of frost coverage. The surface frost sublimates away long after outgassing has ceased because methane is destroyed in the atmosphere by photochemistry. Eventually, the polar caps melt, leaving behind the observed polar seas.

## 1. Introduction

Methane (CH<sub>4</sub>) plays a fundamental role for the climate of Saturn's moon Titan in that it importantly contributes to the greenhouse effect in the troposphere (McKay et al., 1991) and is the most abundant condensable species (Niemann et al., 2005). Furthermore, methane can exist in the troposphere in liquid (rain) or solid (hail, snow) form depending on altitude, or more precisely, temperature and pressure (Graves et al., 2008; Lorenz & Lunine, 2002; Tokano et al., 2006). However, unlike the predominant atmospheric constituent N<sub>2</sub>, methane in Titan's atmosphere is subject to irreversible photochemical loss with a mean lifetime of the order of 10 Myr (Wilson & Atreya, 2004; Yung et al., 1984). This implies that the atmospheric methane content may change on geologic timescales and thereby affect the climate evolution.

Models of Titan's long-term climate evolution developed after the Voyager 1 mission and prior to the Cassini mission typically assumed global-scale hydrocarbon oceans on the surface, which would provide a continuous source of atmospheric methane, and explored how the climate may have changed as the solar luminosity increased (Lorenz et al., 1999; Lunine & Rizk, 1989; McKay et al., 1993). These studies showed that Titan's ocean surface temperature gradually increases and thereby exsolves a large amount of dissolved N<sub>2</sub> to the atmosphere. However,

© 2021. The Authors.

This is an open access article under the terms of the [Creative Commons Attribution-NonCommercial-NoDerivs License](https://creativecommons.org/licenses/by-nc-nd/4.0/), which permits use and distribution in any medium, provided the original work is properly cited, the use is non-commercial and no modifications or adaptations are made.

such global-scale hydrocarbon oceans did not prove to be true, leaving open the possibility that Titan experienced epochs of cold methane-depleted climate with nitrogen precipitation (Charnay et al., 2014; Lorenz et al., 1997; Wong et al., 2015). Mitri et al. (2019) proposed that the observed sharp-edged depressions with raised rims that are filled with lakes may result from explosive eruptions probably due to phase transitions of liquid  $N_2$  in the shallow subsurface. Since such explosive eruptions can only occur during cold methane-depleted episodes, when atmospheric  $N_2$  can condense out (Mitri et al., 2019), they support the past presence of cold episodes, which are one major prerequisite for our study.

Any methane-depleted episodes in the past must have been followed by periods with substantial methane sources that can explain the present atmospheric methane content considering the photochemical lifetime of methane in Titan's atmosphere. It is unknown from climate proxies etc. when the atmospheric methane content that we observe today was introduced to Titan's atmosphere and by which mechanisms. One possibility is that methane was episodically outgassed in certain epochs due to changes in the interior structure of Titan (Tobie et al., 2006). Possible past cryovolcanoes such as Doom Mons ( $15^\circ\text{S}/40^\circ\text{W}$ ) and Erebor Mons ( $5^\circ\text{S}/36^\circ\text{W}$ ) (Lopes et al., 2013) are examples where outgassing might have occurred.

One possible if not the only consequence of massive methane outgassing into a cold  $N_2$  atmosphere is resurfacing by methane frost deposition (Lorenz et al., 1997). Methane frost with its high albedo and a methane cycle with sublimation and deposition of solid methane may cause a climate regime that is qualitatively different from Titan's present climate.

However, 1-dimensional paleoclimate models (e.g., Lorenz et al., 1997) can only simulate global-mean conditions and the influence of atmospheric dynamics on the climate cannot be properly accounted for. For instance, it is so far unknown when and where methane ice sheets existed on Titan and how they would have interacted with the atmosphere. One particular motivation for paying attention to the cold paleoclimate with possible ice sheets on Titan is the detection of polar seas/lakes by Cassini (e.g., Hayes, 2016), which raises questions about the situation of these seas under substantially methane-rich conditions. It is unknown whether these seas were frozen or liquid, they had similar sizes and locations as the present seas or how they transitioned to the present seas when the methane inventory decreased to the present level.

Addressing the complex interaction between paleoclimate, outgassed methane and surface frost calls for simulations by a global climate model (GCM). While the paleoclimate of methane-depleted Titan (Charnay et al., 2014) and orbitally forced climate variation under the present methane abundance (Lora et al., 2014; Tokano, 2019) have already been simulated, Titan's climate change after episodic methane outgassing in the past has not yet been simulated by GCMs.

In this study we explore how an episodic massive methane outgassing into a previously cold methane-depleted atmosphere would have affected the climate of Titan. The paleoclimate of this specific scenario is simulated by a 3-dimensional GCM to properly take into account the impact of atmospheric dynamics and latitudinal and seasonal variation in the volatile cycle. The study particularly addresses how the evolving methane inventory changes the atmospheric and surface temperature, atmospheric circulation pattern, precipitation and sublimation of methane snow and geographic distribution of surface methane frost.

Section 2 describes the numerical model and its boundary conditions. Section 3 describes the general evolution of the predicted overall climatic evolution. Section 4 presents major characteristics of the climate in different epochs. Section 5 investigates the sensitivity of the results to input parameters (solar luminosity, ice albedo, Titan's rotation rate) on the results. Section 6 discusses the implication of the model results for Titan's climate evolution.

## 2. Methods

### 2.1. Model Outline

A numerical paleoclimate model is developed to investigate how a possible massive methane injection into a past cold  $N_2$  atmosphere would have changed the climate of Titan. We follow a late-stage outgassing scenario after 700 Myr BP described by Tobie et al. (2006) because this model quantitatively predicts time series of input parameters (methane outgassing rate, geothermal heat flux) that are internally consistent to each other and that are necessary for a detailed climate simulation. The model assumes a variable total  $CH_4$  inventory in response to

outgassing and photochemical destruction as well as increasing solar luminosity, while it assumes a constant  $N_2$  inventory in the lack of obvious net production and loss mechanisms of  $N_2$  on Titan within the past 1 Gyr.

This study makes use of the Cologne Titan GCM (Tokano, 2019; Tokano et al., 2001), which is adapted to cold past conditions under consideration. This GCM solves the primitive equations on a sphere using a finite-difference dynamical core adopted from the ARIES/GEOS GCM (Suarez & Takacs, 1995). The intrinsic output of the GCM comprises the zonal wind, meridional wind, vertical wind in pressure coordinates, temperature, surface pressure and mole fraction of tracers (if any), while many other quantities are written out for diagnostic purposes. The model domain extends from the surface up to a pressure level of 0.01 hPa, which approximately corresponds to  $\sim 400$  km under present conditions. This upper boundary pressure level is also used in paleoclimate simulations, but the corresponding altitude changes as with the surface pressure, which depends on the prescribed methane inventory and predicted climate. The GCM contains the global topography map after Corlies et al. (2017) and the same topography is assumed for all past epochs due to lack of secure information about the topography in past epochs.

The GCM treats methane gas as a chemically passive tracer and simulates its advection, condensation, surface deposition and sublimation from the surface. Instead of simulating the outgassing itself, the model prescribes the total methane inventory as a function of time BP and simulates the instantaneous climate of each epoch under this methane inventory. The treatment of the methane volatile cycle is described in Section 2.2.

Radiative forcing is calculated with the spectrally resolved radiative transfer model of McKay, Pollack, and Courtin (1989) that is implemented in the Cologne Titan GCM since its first version (Tokano et al., 1999) and was also used in previous radiative-convective paleoclimate simulations (Lorenz et al., 1997; McKay et al., 1993). Radiative feedback of variable atmospheric methane content and surface albedo change due to sedimentation and sublimation of methane frost on the surface is accounted for. Modifications of the radiative transfer model necessary for application to paleoclimate conditions as well as other updates are explained in Section 2.3.

A continuous (transient) simulation over tens and hundreds of Myr with a GCM is not viable for computational reasons. Therefore, the climate evolution is tracked by analyzing the model output of time-slice experiments of selected epochs between 700 Myr BP and present with intervals ranging between 10 to 100 Myr, with a smaller interval during glaciation and deglaciation. Time-dependent external input data including the methane outgassing rate are described in Section 2.4. The starting condition of each simulation is described in Section 2.5.

## 2.2. Treatment of Methane

The model assumes that the total methane inventory in the atmosphere-surface system underwent long-term variations as a consequence of variable methane outgassing (Tobie et al., 2006). Instead of explicitly simulating the outgassing process, the model predicts the methane cycle under the given methane inventory, which is prescribed for each epoch. This means that the sum of globally integrated mass of atmospheric methane and surface methane frost is conserved in each simulation, whereas the partition of methane between the atmosphere and surface can change during the simulation.

The condensation scheme of atmospheric methane is analogous to that of Tokano et al. (2001) except that liquid binary  $CH_4 - N_2$  is replaced by solid  $CH_4$ . Condensation of liquid binary  $CH_4 - N_2$  mixture as in Titan's present atmosphere does not occur under the assumed conditions since the temperature at the condensation level in the simulated past epochs turns out to be always lower than  $\sim 85$  K, the liquidus temperature of  $CH_4 - N_2$  (Lorenz & Lunine, 2002). Condensation occurs as soon as at some grid point the relative humidity relative to solid pure  $CH_4$  exceeds 100%. The supersaturated portion of methane is precipitated out as methane snow without sublimation and deposited on the surface as methane frost.

The mass budget of surface methane frost at a given point is determined solely by precipitation (snow deposition) and sublimation (snow ablation), that is,  $dF/dt = P - E$ , where  $F$  is the depth of methane frost,  $P$  is the precipitation rate and  $E$  is the sublimation rate. Further effects that may affect the snow mass balance such as snowdrift or glacial flow are neglected for simplicity in this first methane glaciation model for Titan.

The sublimation rate at the surface is calculated analogously to Tokano et al. (2001) and Tokano (2009) by the bulk-aerodynamic formula as

$$E = \rho_S C_U C_H (q_{sat} - q) W_S f(Ri) \quad (1)$$

where  $\rho_S$  is the air density in the surface layer,  $C_U = \sqrt{0.002}$  is the surface exchange coefficient for momentum,  $C_H = 0.003$  is the surface heat exchange coefficient,  $q_{sat}$  is the saturation specific humidity of  $\text{CH}_4$ ,  $q$  is the specific humidity of  $\text{CH}_4$ ,  $W_S$  is the wind speed in the surface layer and  $f(Ri)$  is the stability function as used in Equations 1 and 2 of Tokano (2009). The saturation specific humidity for  $\text{CH}_4$  is  $q_{sat,CH_4} = 0.582 p_{sat,CH_4} / p$ , where  $p_{sat,CH_4}$  is the saturation vapor pressure of  $\text{CH}_4$  and  $p$  is the atmospheric pressure.

The saturation vapor pressure over solid  $\text{CH}_4$  (in Pa) is calculated after Fray and Schmitt (2009) as

$$p_{sat,CH_4} = 0.117 \times 10^5 \exp \left[ \frac{6.12 \times 10^5}{519} \left( \frac{1}{90.7} - \frac{1}{T} \right) \right] \quad (2)$$

where  $T$  (in K) is the temperature.

The total  $\text{N}_2$  inventory is assumed to have not changed over the past 1 Gyr. This assumption is based on the fact that on Titan  $\text{N}_2$  is chemically much more inert than  $\text{CH}_4$  and this study focuses on the role of the variable methane inventory. The partial pressure of  $\text{N}_2$  ( $p_{N_2,total}$ ) is thus held fixed at the present value (1.441 bar), which is determined from the atmospheric surface pressure (1.467 bar) measured by the Huygens Probe (Fulchignoni et al., 2005) and the vertical profile of atmospheric composition measured by the Huygens Probe (Niemann et al., 2010). Liquid  $\text{N}_2$  cloud formation is possible in Titan's troposphere under cold conditions (Charnay et al., 2014; McKay et al., 1993; Tokano, 2017). However, this effect is neglected since liquid  $\text{N}_2$  is radiatively inactive and the scattering greenhouse effect by  $\text{N}_2$  cloud particles has a generally minor influence on the surface temperature (Charnay et al., 2014).

### 2.3. Radiative Transfer Model

The model of McKay, Pollack, and Courtin (1989) calculates the absorption and scattering of solar radiation by the stratospheric organic haze, absorptions by permitted transitions of  $\text{C}_2\text{H}_6$  (ethane) and  $\text{C}_2\text{H}_2$  (acetylene) in the stratosphere and collision-induced absorption by various combinations of  $\text{CH}_4$ ,  $\text{N}_2$  and  $\text{H}_2$  molecules by a spectrally resolved radiative transfer code. This model approximately reproduced the temperature profiles measured by Voyager 1 and helped understand the greenhouse effect and anti-greenhouse effect in Titan's atmosphere (McKay et al., 1991). Furthermore, the vertical profile of the solar flux measured by the Huygens Probe (Tomasko et al., 2008) was found to be roughly consistent with that predicted by the model of McKay, Pollack, and Courtin (1989).

The surface temperature is predicted with the scheme described in Tokano (2005) considering solar radiation flux absorbed by the surface, net emitted thermal radiation flux including atmospheric back-radiation, sensible heat flux, latent heat flux due to sublimation and geothermal heat flux. Among these energy fluxes only the geothermal heat flux is prescribed as a function of time BP (Figure 1d).

Areas not covered by methane frost are assumed to have a surface visible albedo of  $A = 0.1$ . This is a value characteristic for the present dry surface (Tokano, 2019). The albedo in frost-covered areas is set to a higher value depending on the predicted frost depth. The choice of the albedo as a function of frost depth is guided by an empirical study with terrestrial  $\text{H}_2\text{O}$  snow (Amaral et al., 2017). If the frost depth exceeds 0.14 m, the albedo is  $A = 0.8$ . If the frost depth is shallower than this threshold, the albedo is  $A = 0.4 + 0.4D/0.14$ , where  $D$  is the frost depth (in meter). The sensitivity of model results on the assumed albedo of methane frost is investigated in Section 5.2. The same surface thermal emissivity ( $\epsilon = 1$ ) is assumed for both frost-covered areas and bare soil. The surface thermal inertia is globally set to  $I = 750 \text{ J m}^{-2} \text{ s}^{-1/2} \text{ K}^{-1}$  for both frost-covered areas and bare soil. This value is a characteristic value for present Titan recommended for climate simulations (MacKenzie et al., 2019) and is also close to the representative value ( $800 \text{ J m}^{-2} \text{ s}^{-1/2} \text{ K}^{-1}$ ) assumed for  $\text{CH}_4$  frost in Pluto climate simulations (Bertrand et al., 2019).

Several model parameters of the radiative transfer model are adjusted to make the model applicable to past methane-rich conditions. The haze production rate and  $\text{H}_2$  abundance are expected to linearly scale with the  $\text{CH}_4$  photolysis rate (McKay et al., 1991). Therefore, these two parameters are scaled with the solar luminosity, neglecting possible deviation of the linear relationship when the methane abundance is not optically thick enough in Lyman

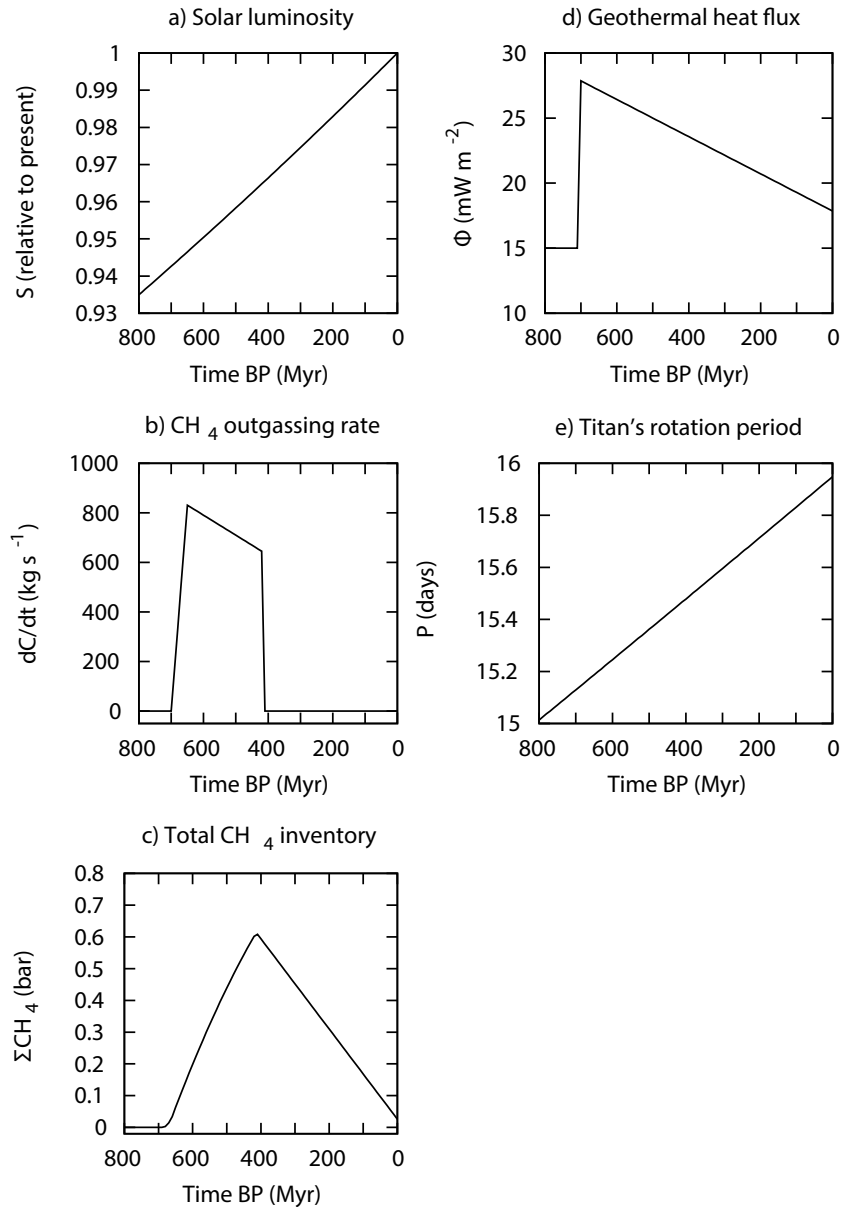


**Figure 1.** Evolution of the input boundary conditions over the past 800 Myr. (a) Solar luminosity relative to present after Gough (1981), (b) Methane outgassing rate after Tobie et al. (2006), (c) Total CH<sub>4</sub> inventory in the atmosphere-ocean system consistent with (b), (d) Geothermal heat flux after Tobie et al. (2006), (e) Titan's orbital/rotational period after Lainey et al. (2020).

$\alpha$ . The haze production rate in the present epoch is set to 0.35 times  $3.5 \times 10^{-14} \text{ g cm}^{-2} \text{ s}^{-1}$  and the uniform H<sub>2</sub> abundance in the present epoch is set to 0.001 (Courtin et al., 2012; Niemann et al., 2010). There is observational evidence of enhanced photodissociation of methane in Titan's thermosphere during solar maximum and modeling evidence of increasing downward flux of C<sub>2</sub> – bearing hydrocarbons such as C<sub>2</sub>H<sub>2</sub> and C<sub>2</sub>H<sub>6</sub> during such episodes (Westlake et al., 2014). Also the photochemical model of Wilson and Atreya (2004) predicts a slightly larger C<sub>2</sub>H<sub>2</sub> abundance during solar maximum. This may imply that the stratospheric C<sub>2</sub>H<sub>2</sub> and perhaps also C<sub>2</sub>H<sub>6</sub> abundances were smaller when the Sun was fainter, all other conditions being equal. Therefore, the constant C<sub>2</sub>H<sub>6</sub> and C<sub>2</sub>H<sub>2</sub> mole fractions in the stratosphere are assumed to scale with the solar luminosity.

In addition, the following temporarily invariable model parameters of the radiative transfer model are changed considering recent information. First, the collision-induced absorption factor for CH<sub>4</sub> – N<sub>2</sub> previously used

turned out to be greatly underestimated (de Kok et al., 2010). This absorption factor is here multiplied by the factor 1.4. This change increases the surface temperature in the present epoch, all other parameters being unchanged. Second, the column haze optical depth in the visible spectrum observed by Huygens (Doose et al., 2016) was shown to be approximately twice as large as in the model of McKay, Pollack, and Courtin (1989). We corrected this bias by dropping the previous assumption that the haze is scavenged by methane condensation and decreased the coagulation factor in the haze model by a factor of 5 and thereby decreasing the sedimentation velocity. This change reduces the sunlight reaching the surface by approximately half and decreases the surface temperature. However, the combination of a larger  $\text{CH}_4 - \text{N}_2$  collision-induced absorption factor and larger haze opacity in the troposphere has a minimal effect on the surface temperature in the present epoch.

#### 2.4. Input Data

There are four external input parameters for this model that are defined as functions of time: Solar luminosity, total methane inventory, geothermal heat flux, and Titan's rotation period.

The evolution of the solar luminosity is adopted from Gough (1981). It steadily increased from 92% the present value at 1 Gyr BP to present (Figure 1a).

The total methane inventory is the most important input parameter and the parameter with by far the largest long-term variation among the four input parameters. It is meant to comprise atmospheric methane and surface methane frost deposits but excludes methane stored in clathrate hydrates. It is assumed to have evolved in the past due to an imbalance between outgassing from the interior and photochemical loss plus escape to space. In this study we consider the evolution model of Titan's interior after Tobie et al. (2006). According to this evolution model, episodic methane outgassing started 700 Myr BP, triggered by upwelling icy plumes after substantial thickening of the icy crust. The outgassing rate peaked 650 Myr BP at 3 times the  $\text{CH}_4$  loss rate ( $831 \text{ kg s}^{-1}$ ), then gradually decreased until 420 Myr BP and eventually ceased (Figure 1b). This results in an increase of the methane inventory between 700 and 420 Myr BP up to 0.61 bar due to outgassing and a linear decrease between 420 Myr BP and the present epoch due to lack of a methane source (Figure 1c). The assumed time evolution is constrained by the present methane inventory (0.0259 bar), which is estimated from the vertical profile of methane mole fraction measured by Huygens (Niemann et al., 2010) and estimated total volume of observed seas and lakes (Hayes, 2016).

The geothermal heat flux is adopted from Figure 3 of the Supplementary Information of Tobie et al. (2006). The heat flux evolved in parallel with methane outgassing. It was negligible prior to 700 Myr BP, then suddenly increased to  $28 \text{ mW m}^{-2}$  at 700 Myr BP and slowly decreased down to  $18 \text{ mW m}^{-2}$  at present (Figure 1d).

Titan's rotation (orbital) period was shorter in the past than today because of Titan's outward migration (Lainey et al., 2020). The evolution of the rotation period is calculated as

$$P = 2\pi \sqrt{\frac{a^3}{GM_S}} \quad (3)$$

where  $a$  is Titan's semi-major axis,  $G = 6.67 \times 10^{-11} \text{ m}^3 \text{ kg}^{-1} \text{ s}^{-2}$  is the universal gravitational constant and  $M_S = 5.6834 \times 10^{26} \text{ kg}$  is Saturn's mass.

The evolution of Titan's semi-major axis  $a$  is adopted from Figure 3 of Lainey et al. (2020), according to which  $a$  increased by 1 Saturn radius during the past 1 Gyr. The portion of the rotation period evolution relevant for this study is depicted in Figure 1e. The rotation period increased from 15.13 days at 700 Myr BP to 15.95 days at present and thereby decreased the Coriolis parameter by 5.4%.

Since the long-term evolution of Saturn's obliquity over the past 1 Gyr is uncertain (Saillenfest et al., 2021), no temporal variation in obliquity is assumed in this model. All simulations are run under Saturn's present obliquity ( $26.7^\circ$ ) and assuming a zero eccentricity of Saturn, that is, the model considers seasonal variations but no seasonal asymmetry.

In the baseline simulations all input parameters are changed simultaneously after Figure 1 (Sections 3 and 4). Additional simulations are carried out to test the sensitivity of the predicted climate evolution to several input parameters (Section 5).

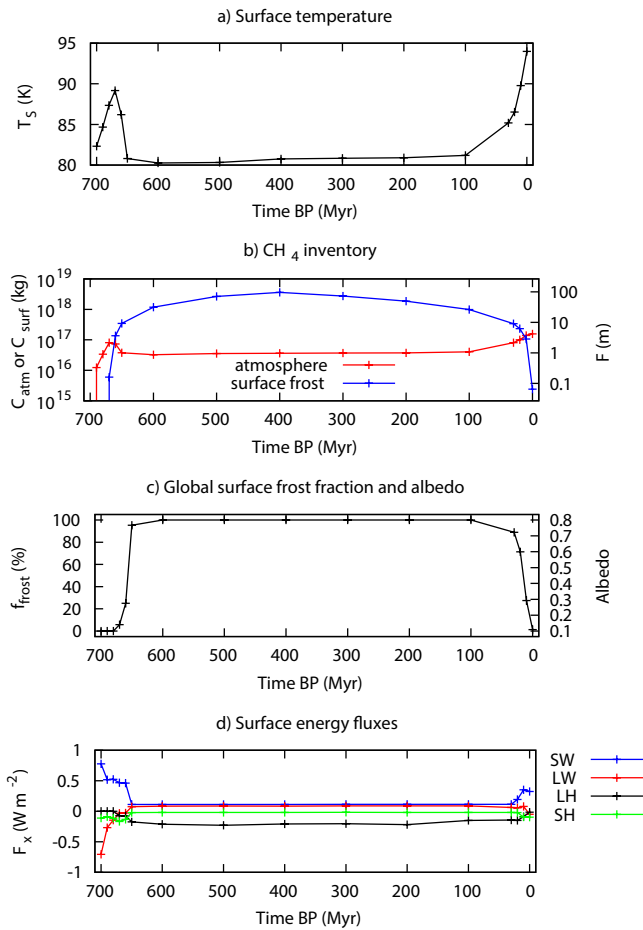


**Figure 2.** Evolution of global-mean annual-mean quantities. (a) Surface temperature, (b) Global methane inventory in the atmosphere and on the surface (left axis) and surface methane frost depth (right axis), (c) Areal fraction of the globe covered by surface methane frost (left axis) and surface albedo (right axis), (d) Surface energy fluxes (SW: absorbed shortwave radiation flux, LW: emitted net thermal radiation flux, LH: latent heat flux, SH: sensible heat flux). Positive energy fluxes are downward. The points on the lines indicate the epochs simulated in this study and the evolution in between is obtained by linear interpolation.

## 2.5. Initialization

All simulations are started from a cold N<sub>2</sub> atmosphere that would have prevailed prior to the last major outgassing since 700 Myr BP. The initial temperature and wind profile are the GCM output for 700 Myr BP predicted under pure N<sub>2</sub> atmosphere. At the beginning of the simulation of each epoch the prescribed total CH<sub>4</sub> inventory after Figure 1c is added to the climate system.

The total CH<sub>4</sub> inventory is partitioned into the atmospheric methane vapor and surface methane frost depending on the initial temperature and pressure profile. The atmospheric CH<sub>4</sub> inventory is limited by saturation (condensation). The initial CH<sub>4</sub> distribution in the atmosphere is uniform from the surface up to the condensation level, then follows the saturation curve up to the top of the condensation layer (highest level with 100% relative humidity) and the CH<sub>4</sub> mole fraction at this level is continued up to the model top. This assumption is based on the vertical profile of methane humidity observed by the Huygens Probe (Niemann et al., 2005, 2010; Tokano et al., 2006). If the outgassed CH<sub>4</sub> inventory is larger than the atmospheric holding capacity of methane, the atmosphere is saturated down to the surface, that is, the relative humidity is 100% from the surface straight up to the top of the condensation layer.

The initial temperature and humidity profile as well as the surface pressure are globally uniform. That portion of the prescribed CH<sub>4</sub> inventory that cannot be held in the atmosphere due to saturation is deposited on the surface as methane frost. In that case the frost is uniformly distributed across the globe at the beginning.

Each simulation is run until the seasonal cycle of the meteorology becomes repeatable and the partition of the methane inventory between atmosphere and surface does not change any more on an annual basis.

## 3. General Evolution of the Predicted Paleoclimate

Before discussing the details of the predicted climate of different past epochs, the general evolution of the predicted paleoclimate since 700 Myr BP is outlined on the basis of baseline simulations. The basic figures are Figure 2, which shows the temporal variation in major global-mean quantities, and Figure 3, which shows global-mean vertical profiles of temperature, methane mole fraction and relative humidity.

Prior to the onset of episodic outgassing, here represented by the results of 700 Myr BP, the atmosphere contains no methane. This makes the atmosphere more transparent to both incoming solar radiation and emitted thermal radiation than the present atmosphere.

The surface absorbs  $\sim 0.8 \text{ W m}^{-2}$  solar radiation (Figure 2d), which is twice as large as on present Titan ( $\sim 0.4 \text{ W m}^{-2}$ , Tomasko et al., 2008) despite the smaller solar luminosity at that time. The net thermal radiation emitted from the surface is also large ( $-0.7 \text{ W m}^{-2}$ ) since the atmospheric back-radiation (greenhouse effect) is weak in the absence of CH<sub>4</sub>, when N<sub>2</sub> – CH<sub>4</sub> collision-induced absorption is absent but only N<sub>2</sub> – N<sub>2</sub> absorption. The resulting global-mean surface temperature ( $\sim 82 \text{ K}$ ) is roughly 10 K lower than at present.

Methane emission after 700 Myr BP gradually increases the methane partial pressure of the atmosphere and thereby reduces both the solar radiation reaching the surface and the net thermal emission, which consists of thermal radiation emitted from the surface and atmospheric back-radiation (greenhouse effect). Since the greenhouse effect by N<sub>2</sub> – CH<sub>4</sub> and CH<sub>4</sub> – CH<sub>4</sub> collisions is more sensitive to the methane abundance than the atmospheric absorption of solar radiation, the increasing methane abundance initially raises the surface and tropospheric temperature relative to a pure N<sub>2</sub> atmosphere. During the first 20 Myr after the start of outgassing, no methane

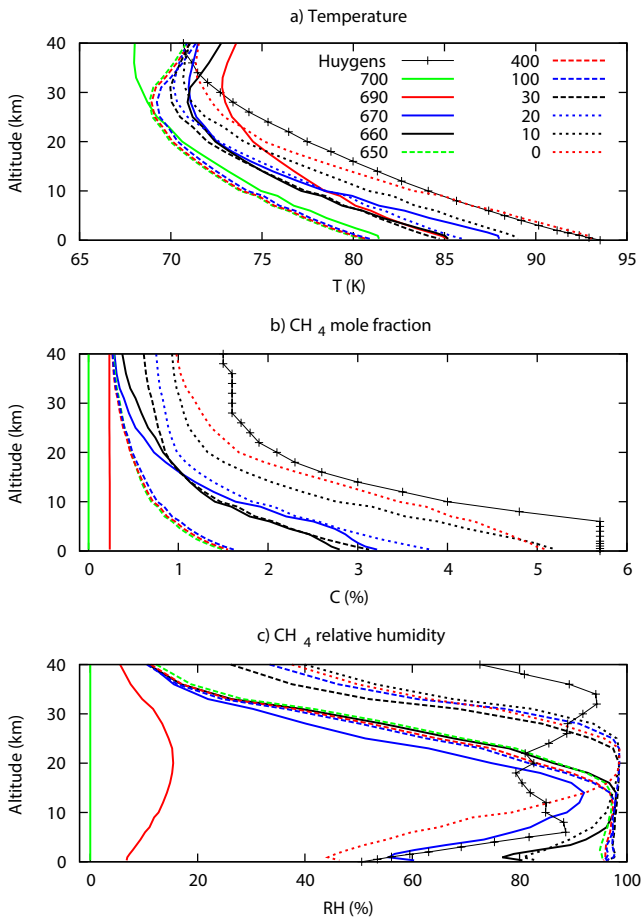


**Figure 3.** Vertical equatorial profiles of temperature,  $\text{CH}_4$  mole fraction and  $\text{CH}_4$  relative humidity (with respect to solid pure  $\text{CH}_4$ ) at the northern vernal equinox ( $L_5 = 0^\circ$ ) in different epochs (in Myr BP). The vertical profiles of the present epoch measured by Huygens (Fulchignoni et al., 2005; Niemann et al., 2010) are also shown for comparison.

condensation occurs because the atmospheric methane abundance is yet too small for methane saturation (Figure 3c). Within these 20 Myr the average surface temperature increases from 82 to 87 K due to increasing greenhouse effect.  $F_{LW}$  turns from negative to positive by the atmospheric back-radiation, while the absorbed solar radiation slightly diminishes due to increasing visible opacity. This period may be regarded as the initial dry state.

After 680 Myr BP the atmospheric methane content becomes large enough to initiate seasonal methane condensation at high latitudes. By 670 Myr BP small permanent polar caps of methane frost appear (Figure 4b). Methane condensation and frost deposition in the polar region begin before the increasing greenhouse effect would have warmed the surface to such an extent that methane snow deposited on the surface would have melted. Once the polar cap becomes perennial, the increased surface albedo regionally decreases the surface temperature by up to 4 K, while the frost-free mid and low latitudes continue to be relatively warm.

With further continuing methane emission, larger portions of the lower troposphere get saturated with methane (Figure 3c). This increases the global extent of ice sheets (Figure 2c) and total mass of surface methane frost (Figure 2b). As long as the entire globe is ice-covered the vast majority of the total methane inventory is deposited on the surface as frost, while the atmospheric methane content changes little due to methane saturation. The limitation of the atmospheric methane partial pressure by saturation in the lower troposphere also limits the greenhouse effect. On the other hand, the high surface albedo of the frost and latent heat flux from the frost-covered surface keeps the surface cold. Therefore, the global-mean surface temperature dramatically decreases down to  $\sim 80$  K once Titan is globally ice-covered (Figure 2a). The temperature in the lower troposphere decreases accordingly (Figure 3a). The cooling of the ice-covered surface and the overlying atmosphere is a manifestation of an ice-albedo feedback.

It is evident that the predicted glaciation and cooling are caused by the increasing methane inventory. The increasing solar luminosity itself would counteract glaciation. Nevertheless, we test the climate sensitivity to the changing solar luminosity in a sensitivity experiment (Section 5.1). The evolving geothermal heat flux is also not responsible for the glaciation. In the absence of liquid hydrocarbon oceans the surface temperature would increase

at 30 K per  $\text{W m}^{-2}$  (0.03 K per  $\text{erg cm}^{-2} \text{s}^{-1}$ ) of additional geothermal heat flux according to McKay et al. (1993) whose radiation code is also used in this model. Hence, a decrease of the geothermal heat flux by 0.01  $\text{W m}^{-2}$  over the past 700 Myr (Figure 1d) decreases the surface temperature by merely 0.3 K over this period, which is 25 times smaller than the predicted surface temperature variation associated with a surface albedo increase after the frost deposition (Figure 2a).

Surface frost advances from high to low latitudes as methane inventory further increases. The surface frost eventually covers the entire globe within 20 to 30 Myr (Figures 2c and 4). The surface absorbs 4.5 times less solar radiation than if the surface is globally ice-covered (Figure 2d). The latent heat flux associated with methane sublimation at the surface amounts to about  $-0.2 \text{ W m}^{-2}$  (Figure 2d) and thereby constitutes the largest surface energy flux. The slightly positive (downward) net thermal emission is caused by the weak thermal emission from a cold surface and the atmospheric back-radiation that overcompensates for the surface thermal emission.

Further outgassing until 420 Myr BP primarily increases the depth of the surface methane frost (Figure 2b), while the surface temperature (Figure 2a), atmospheric temperature (Figure 3a) and the climate as a whole barely change for a very long duration spanning 500–600 Myr. The maximum mean frost depth of  $\sim 100$  m is reached at around 400 Myr BP when the total methane inventory becomes as large as 0.6 bar and outgassing ceases. The climate becomes highly stable once the entire globe is covered by ice sheets. Although the solar luminosity



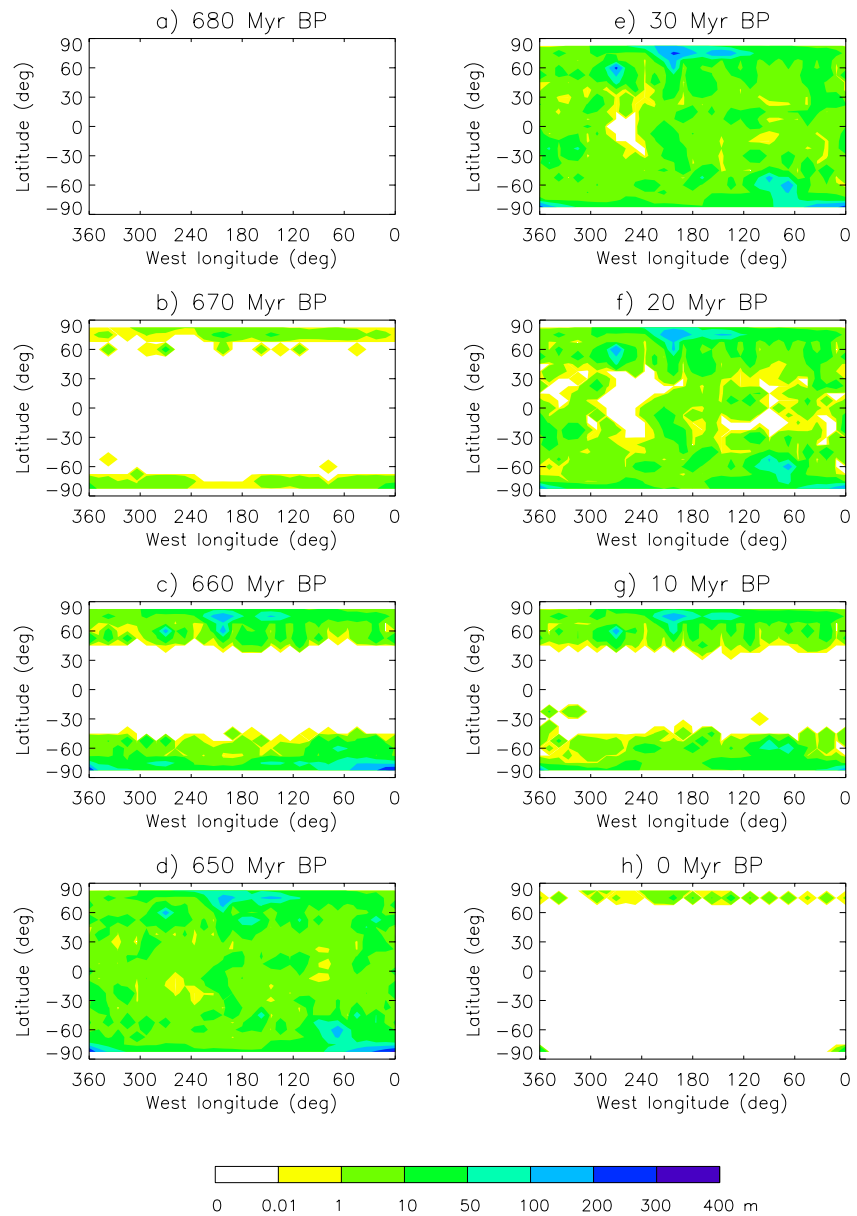


**Figure 4.** Global map of annual-mean surface methane frost depth in eight selected epochs illustrating the phase of surface frost advance (left panels) and surface frost retreat (right panels).

increases by 4.3% between 600 and 100 Myr, the global-mean surface temperature increases by less than 1 K and the atmospheric methane content increases by  $\sim 20\%$ .

Frost ablation begins immediately after the end of outgassing (420 Myr BP) when the total methane inventory begins to decrease due to photochemical destruction in the upper atmosphere. The decreasing atmospheric methane content drives the ablation of surface frost globally. However, it takes nearly 400 Myr after the end of outgassing until ice-free areas appear. The retreat of surface frost to high latitudes (Figure 4h) is accompanied by a strong temperature increase by 10 K (Figure 2a). This temperature increase is a combined effect of the lowering of the surface albedo, which increases the solar radiation absorbed by the surface, increasing atmospheric methane content due to frost ablation, which strengthens the greenhouse effect, and also increasing solar luminosity.

In the following section, we describe the climate of different epochs in more detail.

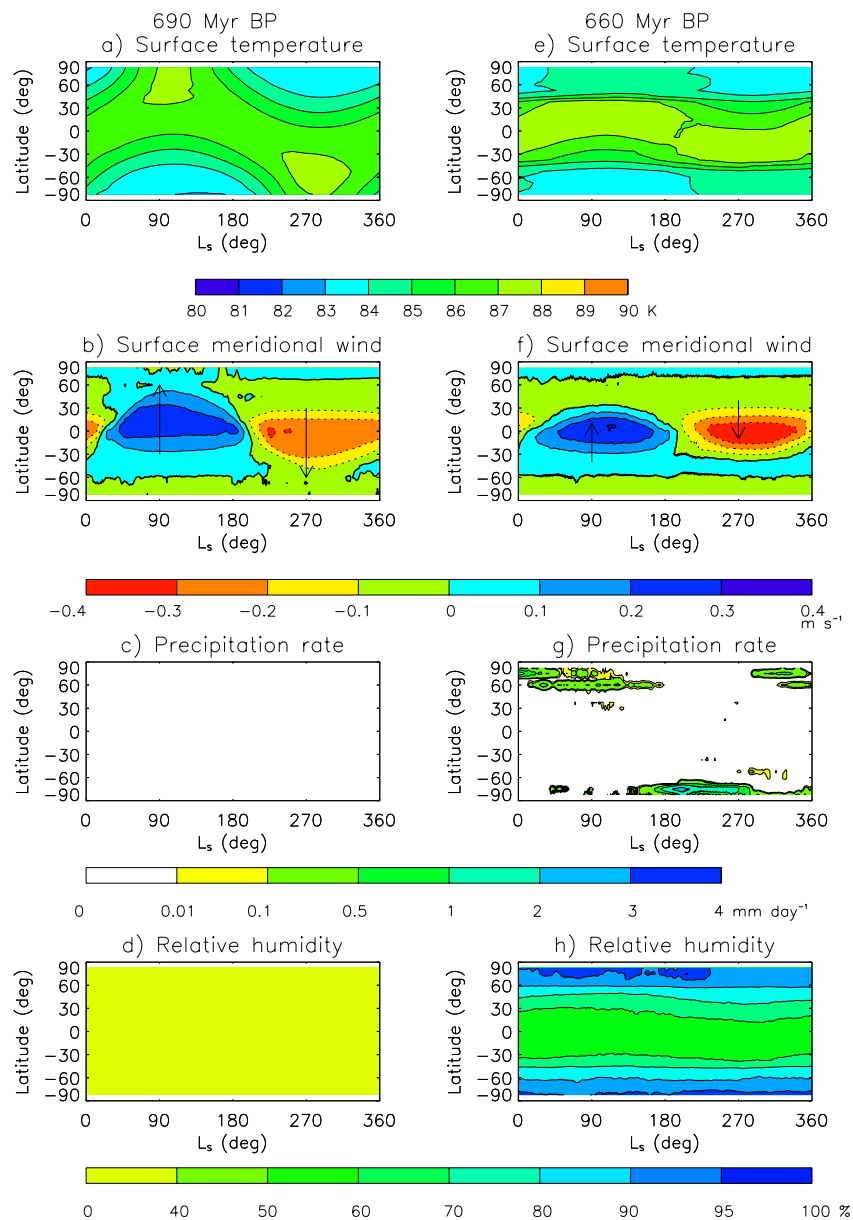


**Figure 5.** Season-latitude section of longitudinally averaged surface temperature, surface meridional wind (positive northward), precipitation rate and surface  $\text{CH}_4$  relative humidity at 690 and 660 Myr BP.

## 4. Paleoclimate of Different Epochs

### 4.1. Climate in the Early Dry State

The first 20 Myr after the onset of massive outgassing (700–680 Myr BP) with a total methane inventory of less than 0.01 bar may be described as the early dry state in that the climate is not affected by methane condensation. The results of 690 Myr BP depicted on the left column of Figures 5 and 6 are representative of this state. Outgassed methane is uniformly mixed in the entire atmosphere (homosphere) (Figure 6b) since there is no mechanism such as condensation to cause a spatial gradient in the methane mole fraction. Consequently, there is no precipitation, no sublimation and no surface frost deposits anywhere.

The surface energy balance is essentially determined by the solar radiation absorbed by the surface and net thermal radiation emitted from the surface, with a minor contribution from the sensible heat flux (Figure 2d). The vertical temperature gradient is more gentle than in the present epoch (Figure 3a) because the greenhouse

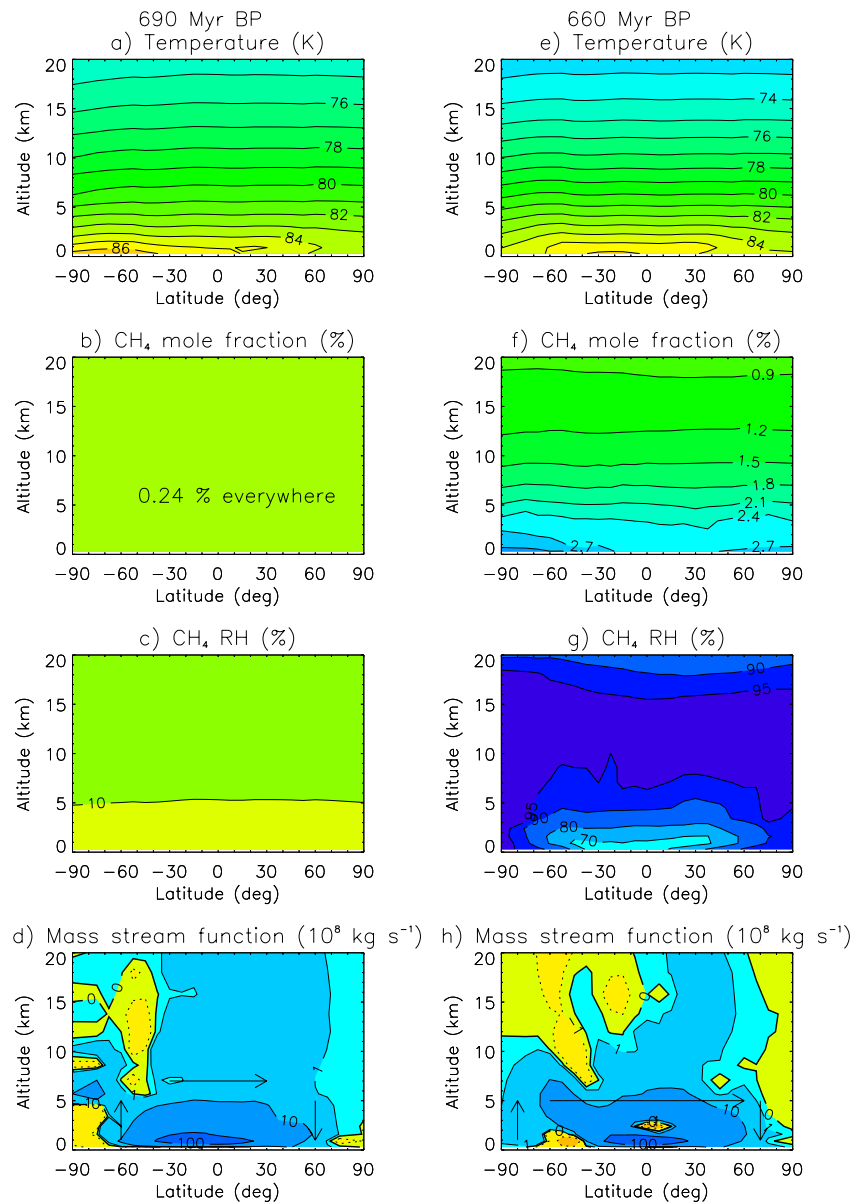


**Figure 6.** Latitude-altitude section of zonal-mean temperature,  $\text{CH}_4$  mole fraction,  $\text{CH}_4$  relative humidity and mass stream function in the lower troposphere at the northern winter solstice ( $L_s = 270^\circ$ ) at 690 and 660 Myr BP. The meridional circulation is clockwise in areas with positive mass stream function.

warming of the near-surface air is weaker. The meridional heat transport in the atmosphere largely takes place in the form of sensible heat (Figure 7a), while the meridional latent heat transport is negligible due to the small moisture (Figure 7b). The annual range of surface and near-surface temperature generally increases with latitude (Figures 5a and 6a). The meridional surface temperature gradient is larger in winter than in summer. The difference between the summer maximum and winter minimum surface temperature amounts to 4–5 K (Figure 5a). The annual-mean equator-to-pole surface temperature difference is smaller (2 K) than in a pure  $\text{N}_2$  atmosphere (700 Myr BP). This is because the atmospheric back-radiation, which is stronger in this epoch than before methane outgassing, is less latitude-dependent than the incoming solar radiation. The predicted slight hemispheric asymmetry in the polar region is not caused by Saturn's eccentricity (which is zero in this model) but is a minor indirect effect of topography, which is asymmetric about the equator.

The meridional circulation essentially consists of a single Hadley-type thermally direct circulation that extends from the high latitudes of the winter hemisphere straight to the summer pole (Figures 5b and 6d). This

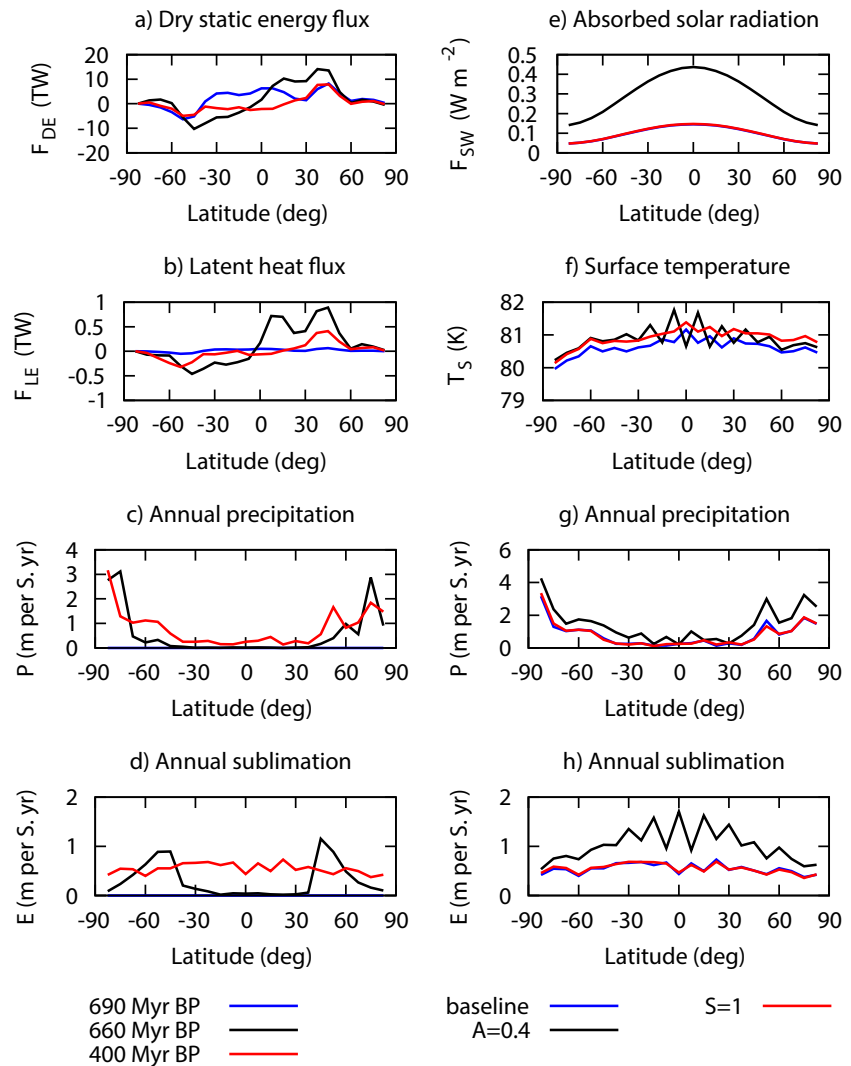


**Figure 7.** Left: Latitudinal profiles of meridional transport (positive northward) of dry static energy and latent heat and annual precipitation and sublimation in the initial dry state (690 Myr BP), partial glaciation state (660 Myr BP) and global glaciation state (400 Myr BP). Right: Latitudinal profiles of longitudinally averaged annual-mean solar radiation absorbed by the surface, surface temperature, annual precipitation and annual sublimation at 400 Myr BP. Results are shown for the baseline simulation (Simulation No. 9) and simulations with increased solar luminosity ( $S = 1$ , Simulation No. 10) and reduced frost albedo ( $A = 0.4$ , Simulation No. 11). In panel e the red and blue curves differ by only  $0.002 \text{ W m}^{-2}$  from each other.

circulation reverses semi-annually around the equinoxes. Small thermally indirect circulations are confined to the polar region. The magnitude of the meridional circulation is comparable to that predicted for the present epoch (Tokano, 2019).

The early dry state discussed here may be different in the vicinity of active volcanoes. While substantial methane snowfall with surface frost deposits begins only 20–30 Myr after the onset of outgassing, methane snowfall could begin much earlier in the vicinity of active volcanoes analogously to  $\text{SO}_2$  snowfall in the vicinity of Io's volcanoes (Geissler, 2003). In the early stage the greenhouse warming of the atmosphere by methane is yet too weak and the methane-enriched air may not be substantially diluted by the global circulation. However, it could also be that surface frost in the vicinity of volcanoes melts or sublimates soon due to locally increased geothermal heat. Such local effects are difficult to simulate with this GCM because of the coarse grid resolution and are disregarded in this study.

#### 4.2. Climate in the Partially Ice-Covered State

The second stage lasting from 670 to 650 Myr BP with a total methane inventory of 0.01–0.1 bar may be described as the partially ice-covered state. This state is characterized by permanent ice sheets poleward of a certain latitude (snow line) and frost-free low latitudes. This situation is qualitatively analogous to that of present Earth and Mars whose poles are covered by polar caps of ice sheets. The results for 660 Myr BP (right columns of Figures 5 and 6) are representative of this state.

The atmospheric methane abundance in this state is large enough for the occurrence of methane condensation in parts of the troposphere. Methane condensation occurs primarily in the polar region where the temperature is slightly lower than at lower latitudes and upward methane transport takes place in spring and summer. Condensation occurs within the altitude range 5–20 km, somewhat depending on season (Figure 6g), and at temperatures between 73 and 82 K (Figure 6e), which cause methane snow instead of methane rain. The decrease of the methane mole fraction with altitude is a consequence of condensation (Figure 6f).

In either polar region methane snowfall occurs primarily in spring and summer and there is a dry season in autumn (Figure 5g). In these seasons and areas methane is transported upward toward the condensation level by the upward branch of the mean meridional circulation. The precipitation rate is less than 1 mm day<sup>-1</sup> in most seasons but occasionally exceeds 2 mm day<sup>-1</sup> in early spring. Snowfall rarely occurs at low latitudes. When this occurs, the snow on the surface sublimates soon, so that there is no permanent surface frost there (Figure 4c). The annual snowfall increases from zero at low latitudes to up to 3 meters per Saturn year in the polar region (Figure 7c). The annual sublimation is zero at low latitudes where there is essentially no snowfall and amounts up to 1 m per Saturn year at high latitudes (Figure 7d). Permanent frost deposits are confined to the polar region (Figures 4a–4c). The polar frost depth varies with season by ~1 m, with a maximum in late summer. The mechanism for the longitudinal variation in the surface frost distribution seen on the global maps (Figure 4) is discussed in Section 4.3.

The presence of permanent polar caps of methane frost significantly affects the surface temperature. While frost-free areas at low latitudes maintain a relatively high surface temperature (~87 K), the polar region becomes colder than in the early dry state because of the high albedo of permanent frost deposits, which cools down the surface (Figure 5e). Consequently, a relatively large meridional surface temperature gradient exists at the surface along the frost boundary (near 50° latitude at 660 Myr BP). Such a gradient is also found in the near-surface atmosphere, but it nearly disappears above 2 km altitude (Figure 6e).

Partial ice sheets affect the meridional circulation pattern as well. The cross-equatorial mean meridional circulation is slightly stronger than in the early dry state but has a narrower latitudinal extent (Figures 5g and 6h). The large meridional temperature gradient along the frost boundary prevents the meridional cell from extending straight to the poles and thereby causes relatively strong thermally indirect cells in either polar region in all seasons. One consequence of this meridional circulation pattern is the relatively inhomogeneous meridional methane distribution near the surface compared to higher altitudes. The meridional heat flux in the atmosphere is still dominated by dry static energy flux but a clear poleward flux of latent heat (Figure 7b) can also be recognized.

In many regards, the climate of the partially ice-covered state can be understood as a colder version of the present climate in that polar seas are replaced by frozen polar caps and rainfall is replaced by snowfall. A major difference, however, is the absence of equatorial precipitation around the equinoxes that was observed by Cassini (Turtle et al., 2018). A likely reason for this difference is that the cross-equatorial meridional circulation does not extend to moist high latitudes. Consequently, little seasonal equatorward transport of moisture from high latitudes can take place and the equatorial areas remain perennially dry (Figure 5h).

This climate state prevails not only during the episodes of frost advance but also during the frost ablation that follows the lengthy ice age. The basic features of the climate during the frost ablation are similar to that during the frost advance, but given the higher solar luminosity, the temperatures tend to be higher than in previous epochs (Figure 2).

#### 4.3. Climate in the Snowball State

The third phase of climate variation after the onset of massive outgassing is reached between 650 and 600 Myr BP when the total methane inventory exceeds ~0.1 bar. The methane inventory is then too large to store it entirely in

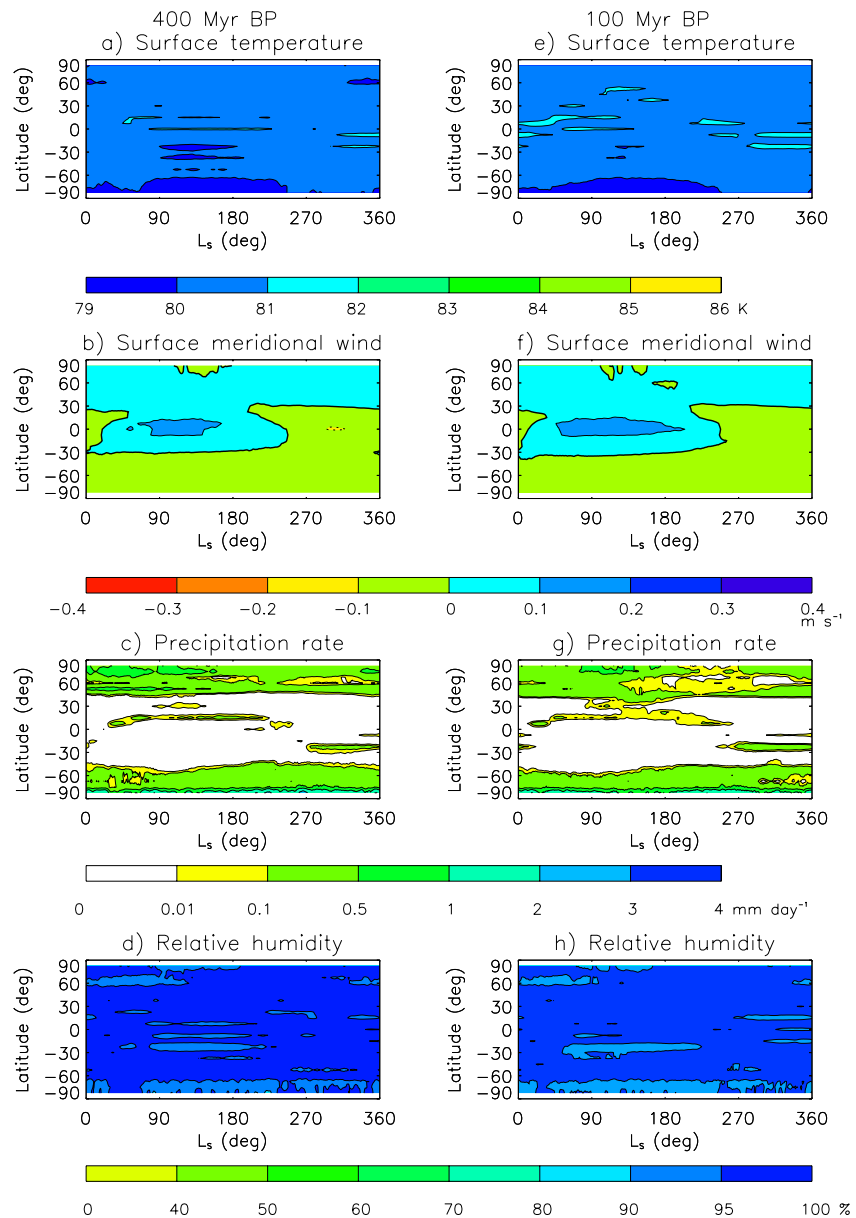


**Figure 8.** Same as Figure 5 for 400 and 100 Myr BP.

the atmosphere and in parts of the globe, so that the entire globe is covered by a methane frost cover. Titan under this condition may be referred to as the methane snowball Titan by analogy with Earth's Neoproterozoic snowball (Hoffman et al., 1998). The results for 400 and 100 Myr BP (Figures 8 and 9) are representative of this state.

The climate in the snowball state qualitatively differs from that of the partially ice-covered or early dry state discussed above in several aspects. The first major characteristic is the very low surface temperature (80–81 K) combined with a small meridional and seasonal variation in surface temperature (Figures 8a and 8e). Also the entire troposphere is colder (Figure 3a) and the meridional temperature gradient is tiny (Figures 9a and 9e).

As a second major characteristic, nearly the entire lower troposphere below 15 km altitude is saturated (Figures 9c and 9g). This can clearly be contrasted to the climate in the partially ice-covered state in which the lower troposphere at low latitudes is dry (Figure 6g). The reason for the global saturation of the lower troposphere is the permanent global frost cover, which causes sublimation whenever the near-surface air gets subsaturated. Given the high relative humidity, precipitation occurs everywhere (Figure 7d), although there are some differences

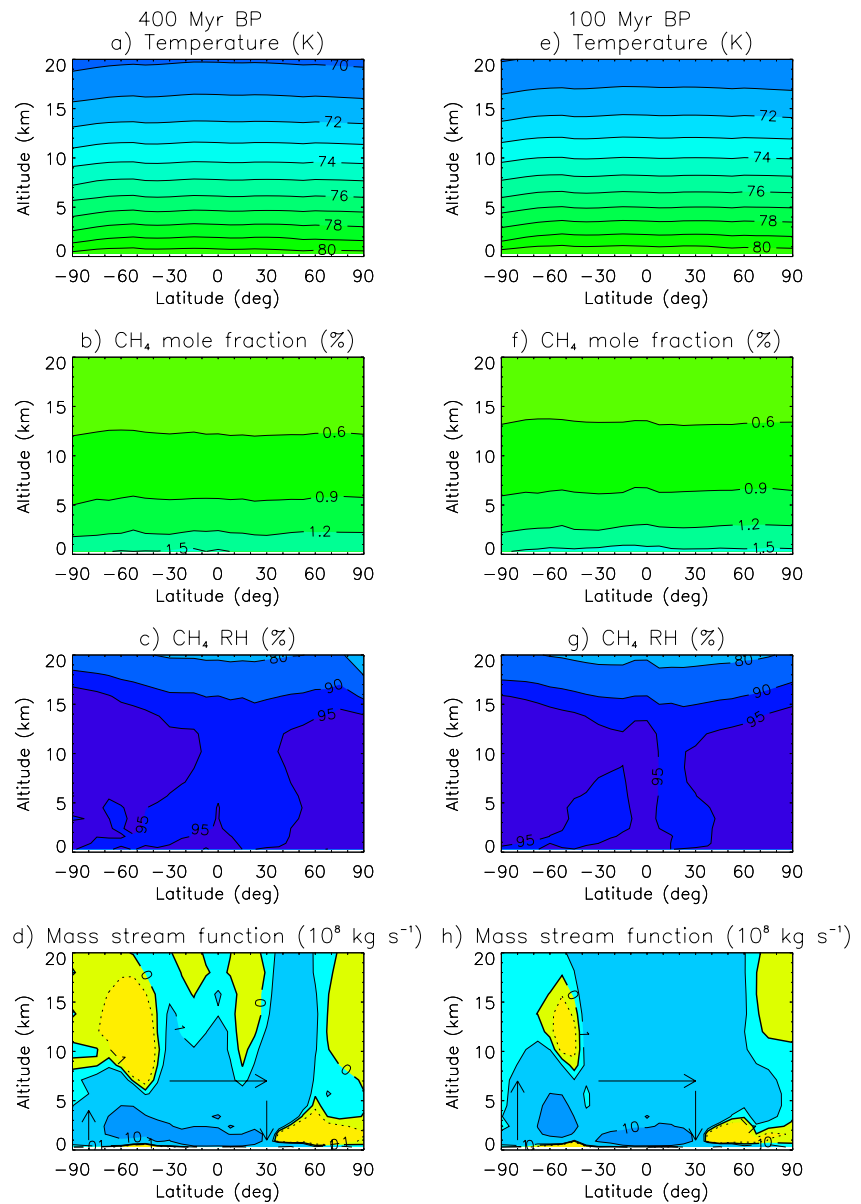


**Figure 9.** Same as Figure 6 for 400 and 100 Myr BP.

between low and high latitudes (Figures 8c and 8g). Precipitation at high latitudes occurs quasi-perennially (Figures 8b and 8f). Nearly continuous polar snowfall occurs because the meridional circulation does not seasonally reverse unlike in the present epoch, so that polar methane is exchanged only between the polar air and polar surface. On the other hand, precipitation at low latitudes occurs mainly in spring and summer, when upward methane transport by the meridional circulation takes place, and there are long snow-free seasons.

The third major characteristic is the relative weakness and seasonal invariance of the meridional circulation. The meridional mass stream function (Figures 9d and 9h) is one order of magnitude smaller than in other epochs. The surface meridional wind (Figures 8b and 8f) is typically three times weaker than in the partially ice-covered state. The weakening of the meridional circulation can basically be ascribed to the small seasonal and meridional variation in surface temperature. As a consequence of the weak meridional circulation, the meridional heat flux is weaker than in other climate states (Figures 7a and 7b).

It is instructive to qualitatively compare the predicted climate of snowball Titan with that predicted for the Neoproterozoic snowball Earth (Pierrehumbert et al., 2011), even though they are caused by different mechanisms.

On the one hand, there are some common features between snowball Titan and snowball Earth. First, the low temperature limits the greenhouse effect by the main condensable species (water vapor on Earth and methane vapor on Titan). Second, the hydrological cycle becomes sluggish but ubiquitous. The high relative humidity in large portions of the lower troposphere makes precipitation more frequent and wide-spread, but the slow transport of water vapor (Earth) and methane vapor (Titan) acts to reduce the precipitation rate.

On the other hand, there are also putative differences between the climate regime of Titan and Earth in the snowball state. On snowball Earth the surface thermal inertia drastically decreases when the ocean freezes, resulting in extreme seasonal cycles (Pierrehumbert et al., 2011). By contrast, Titan's surface thermal inertia is unlikely to substantially decrease when the present dry surface is replaced by methane frost. The predicted seasonality on snowball Titan is weaker than on present Titan because of the high surface albedo and unchanged surface thermal inertia.

It may also be useful to consider possible analogies and differences between the simulated snowball Titan and Neptune's moon Triton, which has long been considered a colder counterpart of Titan (McKay, Pollack, Zent, et al., 1989). Current knowledge is that Triton has a tenuous  $N_2$  atmosphere in vapor pressure equilibrium with the bright  $N_2$  frost deposits, photochemical haze production takes place in the atmosphere in the presence of  $CH_4$  and geysers of  $N_2$  vapor are found (Hansen et al., 2021). Frost deposition of the majority of  $N_2$  outgassed from the interior in a wide area due to saturation and surface temperatures below the freezing point is analogous to the simulated frost deposition of outgassed  $CH_4$  on cold Titan. A major qualitative difference, however, is that  $N_2$  on Triton is the main atmospheric component, while  $CH_4$  is the second most abundant atmospheric component on Titan. Therefore, the atmospheric pressure and temperature on Triton globally undergo substantial seasonal variations due to sublimation-condensation cycles (Elliot et al., 1998), supported by the relatively small total  $N_2$  inventory. By contrast, the seasonal variation on snowball Titan is much less significant. Moreover, the huge methane inventory in some past epochs compared to the nitrogen inventory on Triton makes it easier to cover the entire globe by frost deposits.

In summary, the climate of putative globally ice-covered Titan in the past exhibits features, which clearly differs from those of the present climate, and there are both analogies and differences to the climate of snowball Earth.

#### 4.4. Global Distribution of Surface Frost

The model predicts that the surface frost distribution depends on the total methane inventory and is primarily a function of latitude (Figure 4). However, the global frost cover also exhibits longitudinal variations in addition to a clear latitudinal variation. Large snow accumulations tend to occur near the south pole around the  $0^\circ$  meridian, near the north pole around the  $210^\circ W$  meridian, near  $75^\circ N/200^\circ W$  and  $60^\circ S/65^\circ W$  so far these areas are covered by frost. At 400 Myr BP the maximum frost depth on the plateau near the south pole reaches nearly 400 m, four times larger than the global average (Figure 10a).

The only external factor that can produce longitudinal variability in this model is global-scale topography. All other input parameters are geographically uniform or non-dimensional. A comparison of the frost map with the topography map (Figure 10b) reveals that the frost generally tends to be deeper on elevated terrains, while the frost in topographic basins is shallower.

Two effects contribute to local snow accumulation on plateaus. The first, more important effect is the slightly lower air temperature over elevated terrains (Figure 10c), which decreases the sublimation rate of the surface frost compared to low-elevation areas. The second effect is the geographic variability in surface wind pattern by large-scale topography. While the longitudinally averaged surface wind pattern is controlled by the seasonal cycle and latitudinal frost distribution as already described, the longitudinal variation in annual-mean surface wind (Figure 10d) is caused by topography. The globally fastest surface wind is found near the south pole around the  $0^\circ$  meridian, where there is a relatively steep topography variation between the basin of Hagal Planitia and the south polar plateau and thereby induces a strong poleward surface flow. This flow causes an enhanced convergence of near-surface air and subsequent upwelling over the plateau, which causes a local maximum of condensation and snowfall. Such an effect may be referred to as the blocking effect of orography (Houze, 2012). Importantly, the strong poleward flow is upslope wind and is not katabatic wind over snow. Enhanced convergence of surface wind due to topography is also found near the north pole between  $120^\circ W$  and  $210^\circ W$  and this also causes a larger snow accumulation compared to other longitudes, yet the effect here is less pronounced than near the south pole.



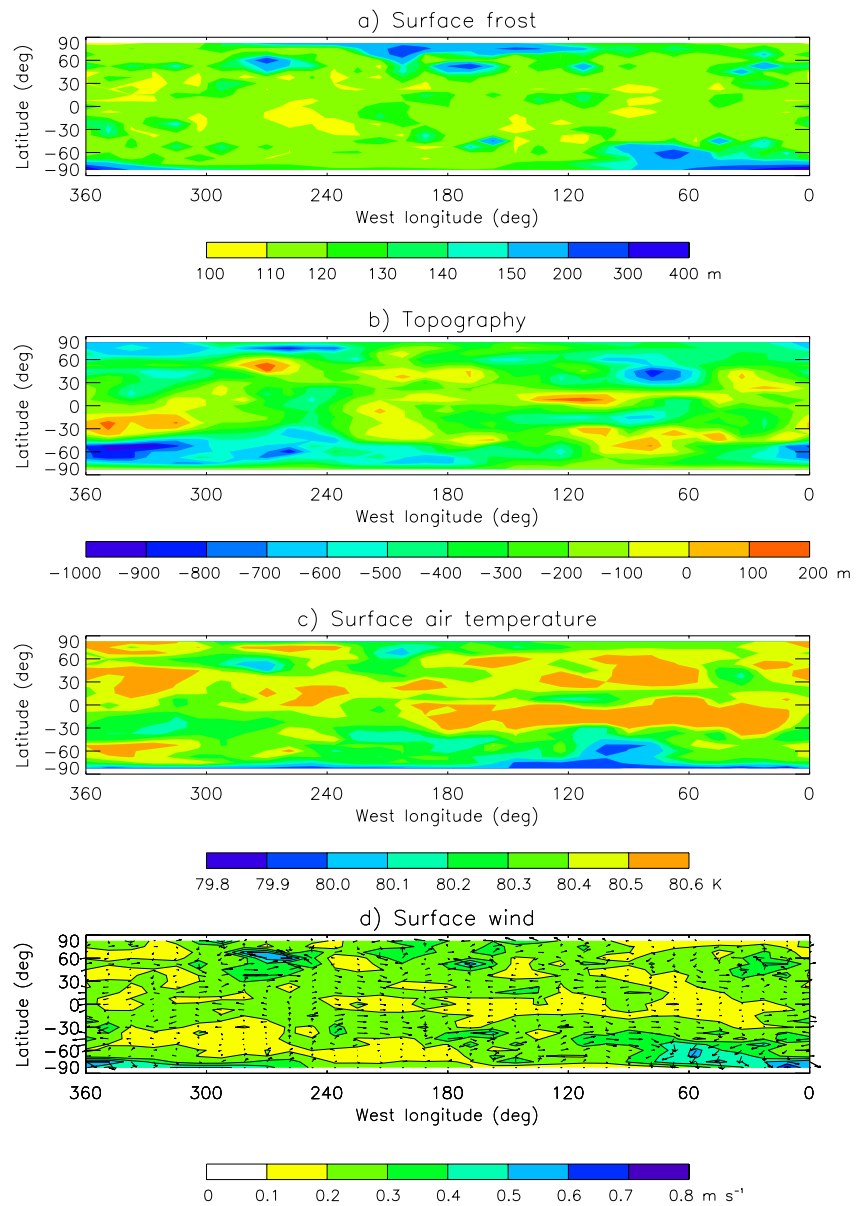


**Figure 10.** Global maps of annual-mean surface methane frost depth, topography after Corlies et al. (2017), surface air temperature and surface wind at 400 Myr BP.

However, the predicted strong snow accumulation on plateaus should be regarded with caution. Potentially important effects such as snowdrift or glacial flow that are likely to play some role in the presence of topography are not simulated in the current model. Therefore, snow accumulation on plateaus may in reality be less pronounced than in the model prediction. Likewise, basal melting of thick frost deposits may reduce the thickness of the frost.

Another point to note is that Titan's topography may not have been invariant over the entire duration under consideration. For instance, Titan's topography may have been flatter hundreds of Myr ago because the ice shell was thinner (Nimmo & Bills, 2010), the cumulative polar ethane precipitation was smaller in the past (Choukroun & Sotin, 2012) or the processes shaping Titan's outer shell are strongly influenced by the atmosphere and dynamics of the subsurface ocean (Čadek et al., 2021). If the topography was flatter in the past, the predicted methane frost distribution may have been more longitudinally uniform than shown in Figure 4.

**Table 1**

*Summary of Simulations and Their Results Including Sensitivity Experiments: A (Frost Albedo), S (Solar Luminosity), P<sub>rot</sub> (Titan's Rotation Period), T<sub>s</sub> (Annual-Mean Global-Mean Surface Temperature), C<sub>atm</sub> (Atmospheric Methane Inventory), C<sub>surf</sub> (Surface Methane Inventory), f<sub>frost</sub> (Global Areal Fraction Covered by Surface Frost)*

No.	Time (Myr BP)	A	S	P <sub>rot</sub> (days)	T <sub>s</sub> (K)	C <sub>atm</sub> (kg)	C <sub>surf</sub> (kg)	f <sub>frost</sub> (%)
1	0	0.8	1.000	15.945	93.99	1.57 × 10 <sup>17</sup>	2.42 × 10 <sup>15</sup>	1.3
2	0	0.8	0.94	15.945	92.58	1.53 × 10 <sup>17</sup>	6.26 × 10 <sup>15</sup>	5.8
3	10	0.8	0.999	15.934	89.78	1.40 × 10 <sup>17</sup>	1.07 × 10 <sup>17</sup>	27.5
4	20	0.8	0.998	15.923	86.39	1.01 × 10 <sup>17</sup>	2.33 × 10 <sup>17</sup>	71.3
5	30	0.8	0.997	15.911	85.08	8.10 × 10 <sup>16</sup>	3.40 × 10 <sup>17</sup>	89.0
6	100	0.8	0.991	15.830	81.05	3.84 × 10 <sup>16</sup>	9.93 × 10 <sup>17</sup>	100.0
7	200	0.8	0.991	15.713	80.91	3.75 × 10 <sup>16</sup>	1.87 × 10 <sup>18</sup>	100.0
8	300	0.8	0.975	15.595	80.83	3.70 × 10 <sup>16</sup>	2.74 × 10 <sup>18</sup>	100.0
9	400	0.8	0.966	15.467	80.75	3.64 × 10 <sup>16</sup>	3.61 × 10 <sup>18</sup>	100.0
10	400	0.8	1.0	15.467	81.09	3.87 × 10 <sup>16</sup>	3.61 × 10 <sup>18</sup>	100.0
11	400	0.4	0.966	15.467	81.16	3.63 × 10 <sup>16</sup>	3.61 × 10 <sup>18</sup>	100.0
12	500	0.8	0.958	15.362	80.32	3.57 × 10 <sup>16</sup>	2.66 × 10 <sup>18</sup>	100.0
13	600	0.8	0.950	15.245	80.25	3.27 × 10 <sup>16</sup>	1.19 × 10 <sup>18</sup>	100.0
14	650	0.8	0.947	15.187	80.80	3.77 × 10 <sup>16</sup>	3.46 × 10 <sup>17</sup>	95.3
15	660	0.8	0.946	15.176	86.20	7.32 × 10 <sup>16</sup>	1.36 × 10 <sup>17</sup>	24.9
16	670	0.8	0.945	15.164	89.16	8.12 × 10 <sup>16</sup>	6.01 × 10 <sup>15</sup>	5.7
17	680	0.8	0.944	15.152	87.34	3.40 × 10 <sup>16</sup>	0.0	0.0
18	690	0.8	0.943	15.141	84.68	1.23 × 10 <sup>16</sup>	0.0	0.0
19	690	0.8	0.943	15.945	85.98	1.23 × 10 <sup>16</sup>	0.0	0.0
20	700	0.8	0.943	15.129	82.32	0.0	0.0	0.0

*Note.* Underlined simulation numbers and parameters refer to sensitivity experiments (Section 5).

## 5. Sensitivity to Input Parameters

In the baseline simulations presented in Sections 3 and 4 several input parameters are changed simultaneously as a function of time (Figure 1). In addition, the albedo of methane frost is intrinsically uncertain. In this section we perform additional simulations for selected epochs to elucidate the relative importance of these factors for the climate evolution and causal relationship between the external forcing mechanism and climate change. These simulations and their major results are summarized in Table 1.

### 5.1. Solar Luminosity

An additional simulation (Simulation No. 10) is run for 400 Myr BP with the present solar luminosity ( $S = 1$ ) instead of the real solar luminosity of that epoch ( $S = 0.9664$ ). The increased solar luminosity increases the solar radiation absorbed by the surface, which in turn globally raises the surface temperature and sublimation rate. This increases the surface temperature by  $\sim 0.3$  K globally (Figure 7f and Table 1) but otherwise causes little change in meteorology or global frost distribution.

The solar luminosity is more important for the climate evolution in epochs in which the majority of Titan's surface is not covered by frost. In these epochs the difference in the solar radiation absorbed by the surface has a larger dependence on the solar luminosity thanks to a low surface albedo. For instance, the global-mean surface temperature in the present epoch is 93.5 K in the baseline simulation (Simulation No. 1). The polar surface temperature in summer approaches the melting point of methane (Figure 12c). If, however, a reduced solar luminosity of  $S = 0.94$  (corresponding to the value  $\sim 700$  Myr BP) is assumed, the global-mean surface temperature is  $\sim 1$  K lower (Simulation No. 2). This difference matters for the melting of the polar cap discussed in Section 6.1. Moreover, an approximately three times larger polar cap would have survived up to the present day if hypothetically

the solar luminosity did not increase since then. Nevertheless, the solar luminosity increase is not the major driver of frost ablation over the past 30 Myr.

### 5.2. Frost Albedo

Next, an additional simulation (Simulation No. 11) for the same epoch is run with a lower frost albedo (0.4 instead of 0.8). Such an albedo decrease could be caused by aging of snow after the end of outgassing or sedimentation of dark organic material condensed out from the atmosphere.

This albedo change increases the solar radiation absorbed by the surface frost globally by a factor of 3. Most of the additional energy input is consumed by the sublimation of surface frost. The annual sublimation increases by a factor of a few, especially at low latitudes (Figure 7h). The zigzag of the latitudinal profile reflects the topographically caused geographic variation in sublimation rate. In accord with the increasing sublimation rate, the precipitation rate also increases by a similar factor globally (Figure 7g). This means that a lower frost albedo makes the hydrological cycle more vigorous. Also the surface temperature slightly increases but this trend is counterbalanced by increased latent heat flux, that is, sublimation cooling (Figure 7f).

### 5.3. Titan's Rotation Period

The rotation period of a planet/moon directly affects the atmospheric dynamics via the Coriolis force, which scales with the rotation rate. The baseline simulations take into account the gradual increase of the rotation period by 5.4% from 15.129 days (rotation rate of  $4.807 \times 10^{-6} \text{ s}^{-1}$ ) to 15.945 days (rotation rate of  $4.561 \times 10^{-6} \text{ s}^{-1}$ ) over the past 700 Myr. Here we run an additional simulation (Simulation No. 19) for 690 Myr BP (as an example) with the present rotation period instead, which is 5% longer than in the baseline simulation.

The simulation shows that the variation in Titan's rotation rate does not qualitatively change the global pattern of temperature, zonal and meridional circulation (Figure 11). Only minor changes in the strength of zonal and meridional circulation at high latitudes can be recognized. The impact of rotation rate variations is likely to be even smaller in the more recent, partially or globally ice-covered state when the rotation rate was even closer to the present one. Therefore, the large seasonality of the climate at 690 Myr BP can clearly be ascribed to the small atmospheric methane content and not to Titan's faster rotation rate in this epoch.

## 6. Discussion

### 6.1. Frost Ablation

Present Titan is not known to have a perennial methane snow cover on scales that can be resolved by Cassini's imaging instruments. Only possible temporary frost deposits may exist after rainfall and subsequent evaporative cooling (Barnes et al., 2013). This implies that methane frost ablation must have taken place in the past if Titan's surface was ever covered by methane frost. For computational reasons it is not feasible to run the GCM continuously for hundreds of simulated Myr under steadily varying boundary conditions and to create an animation of frost ablation. Nevertheless, the sequence of global surface frost maps (right panels of Figure 4) and their latitudinal profiles (Figure 12b) obtained from time-slice experiments gives an impression of how frost ablation on Titan may have proceeded.

Basically, frost ablation occurs in the reversed order as frost advance, that is, areas that became ice-covered later than other areas lose the frost earlier because the frost cover to remove is thinner. Frost ablation occurs everywhere when the near-surface relative humidity decreases. After the onset of frost ablation the frost cover becomes thinner globally but it takes 350–400 Myr until the first frost-free areas appear in topographically depressed areas at low latitudes. The first region that gets ice-free according to this model is Belet (240–270°W) near the equator that is currently covered by sand dunes. The second major area of early frost ablation is Xanadu, also near the equator. Thereafter, surface frost retreats from low to high elevations and from low to high latitudes. For the present epoch the model predicts thin patchy polar caps near the north pole (up to 21 m) and a small polar cap at the south pole (Figure 4h).

In the equatorial region where sand dunes were observed by Cassini (Lorenz et al., 2006), our model predicts frost deposition to have started between 660 and 650 Myr BP and the last frost deposits to have disappeared between

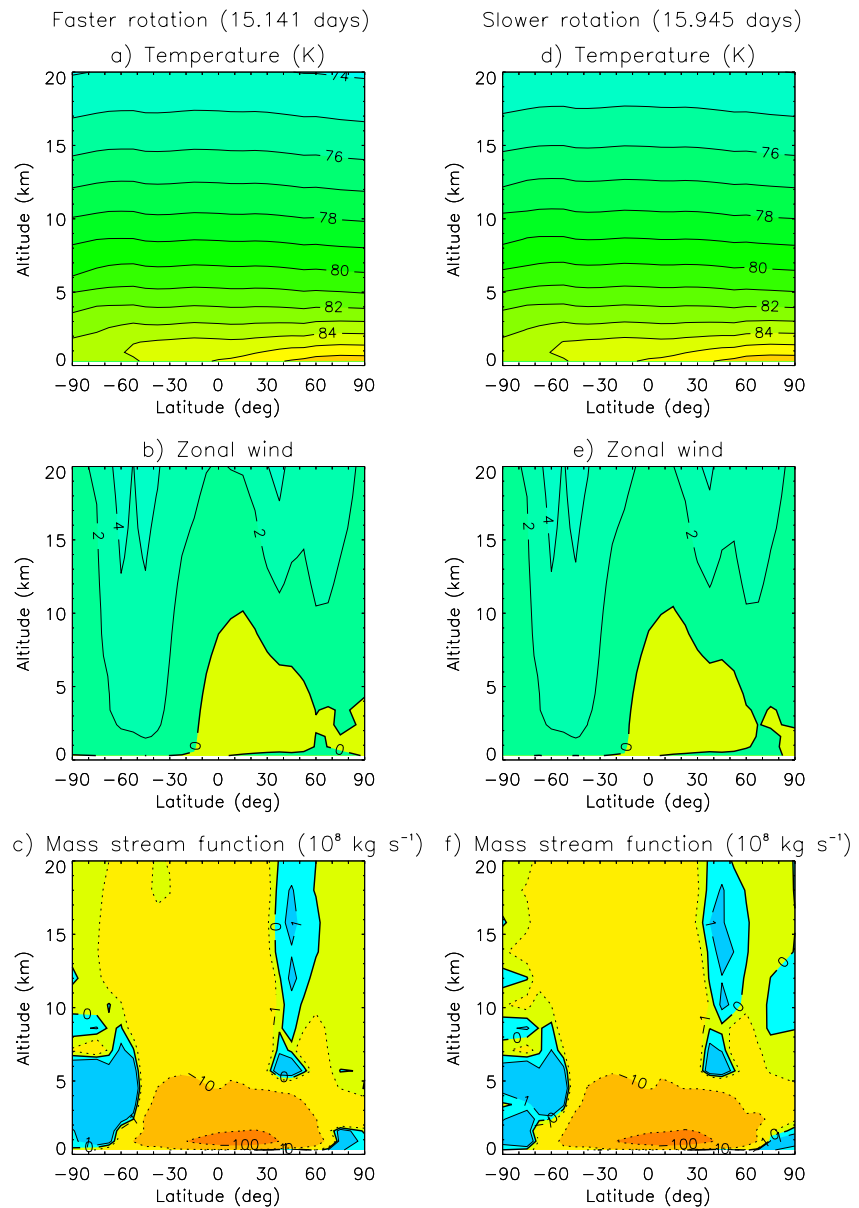


**Figure 11.** Comparison of temperature, zonal wind and mass stream function at  $L_s = 90^\circ$  at 690 Myr BP simulated under two different rotation periods of Titan (past 15.141 days vs. present 15.945 days).

20 and 10 Myr BP (Figure 4). If the dune material already existed prior to possible methane frost deposition, it would have been buried and thus immobile (except for possible glacial flows) during this lengthy period. Even though some of the organic material that constitutes the sand dunes might be older, the present equatorial dunes would have formed only after the last frost ablation at low latitudes, that is, within the past 10–20 Myr, so that the sand was exposed to winds. The reorientation of Titan's dunes is estimated to have occurred on timescales of 100 kyr to 1 Myr (Ewing et al., 2015). Thus, the predicted recent 10–20 Myr ice-free periods at low latitudes should be long enough for the formation of observed dunes.

## 6.2. Melting of Polar Caps

Titan's polar region contains numerous hydrocarbon seas and lakes, especially near the north pole (Hayes, 2016). They cover a total area of  $9 \times 10^5 \text{ km}^2$ , which corresponds to 1% of Titan's global surface area. The observed seas are found between  $225^\circ\text{W}$  and  $20^\circ\text{W}$  in the northern hemisphere, with further numerous lakes at nearly all

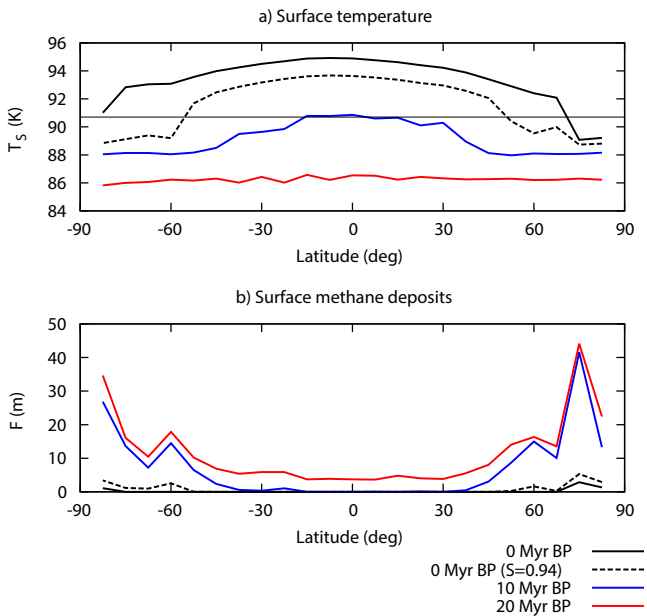


**Figure 12.** Latitudinal profile of longitudinally averaged surface temperature and frozen/liquid surface methane deposits in three recent epochs (0, 10 and 20 Myr BP). Results with hypothetically reduced solar luminosity ( $S = 0.94$ ) in the present epoch are also shown for comparison. The thin horizontal line at 90.7 K indicates the melting point of pure  $\text{CH}_4$ .

longitudes north of  $70^\circ\text{N}$ . Lakes in the southern hemisphere are found at  $72^\circ\text{N}/183^\circ\text{W}$ ,  $86^\circ\text{S}/162^\circ\text{W}$ ,  $86^\circ\text{S}/237^\circ\text{W}$ ,  $80^\circ\text{S}/185^\circ\text{W}$ . Several ideas for the origin of the polar seas have been proposed: The polar seas could have been caused by condensation and deposition of atmospheric methane in the polar region (Aharonson et al., 2009). Alternatively, they could be remnants of once larger methane oceans that gradually desiccated due to photochemical destruction of methane in the upper atmosphere (Larsson & McKay, 2013). Possible geologic origins of lake basins are karstic dissolution (Cornet et al., 2015) and near-surface explosion of  $\text{N}_2$  vapor in the shallow subsurface (Mitri et al., 2019).

The model results of the present study offer an opportunity to discuss as to how the present polar seas could be related to frozen polar caps predicted for the recent past. The baseline model for the present epoch predicts frozen polar caps especially near the north pole with a total area corresponding to 1.3% of the globe (Figure 4h), which is consistent with the observations by Cassini. The predicted northern polar cap extends over almost all longitudes and are not confined to the observed locations of Kraken Mare, Ligeia Mare and Punga Mare. The southern polar cap is much smaller. The predicted total mass of the surface methane deposits in the present epoch is  $6 \times 10^{15}$  kg (Table 1). The estimated lower limit of the total sea/lake volume is 70,000  $\text{km}^3$  (Hayes, 2016), which corresponds to a total mass of  $3 \times 10^{16}$  kg assuming a liquid density of  $450 \text{ kg m}^{-3}$ . Hence, the total volume of the predicted polar seas is only half the estimated total volume of the observed seas but the predicted methane deposits are thinner and cover a larger area than observed.

In the recent past (10 Myr BP and less) the frozen polar cap and liquid polar seas turn out to be more extensive in the north than in the south (Figure 12b).

This hemispheric asymmetry is a consequence of Titan's global topography as simulated and explained by Tokano (2019). Therefore, it is conceivable that the frozen polar caps were already concentrated near the north pole before melting and subsequent melting did not change the hemispheric asymmetry of the surface methane distribution.

The approximate agreement of the latitudinal distribution of the observed seas and predicted polar caps gives some credence to the suggestion that the present seas and lakes are a major consequence of melting of former polar caps. The disagreement between the longitudinal distribution of the observed seas and predicted polar caps can be explained by the difference between snow and liquids. Our model does not simulate glacial flow or percolation/drainage of melted polar caps. Therefore, the model tends to predict a thin frost cover in a wide area. In reality, melting snow on elevated terrains would percolate to porous surface or drain to nearby basins. Liquid methane stored in basins can better resist desiccation than thin frost covers since the effective area of evaporation is smaller than that of more wide-spread methane frost. This may explain why the observed seas have a larger mass than the mass of the predicted polar caps that cover a larger area.

We do not argue that the basins themselves are of glacial origin, nor that glacial erosion in the sense understood on Earth has shaped the coasts. Although it has been noted that Moray Sinus appears to be rather deep compared to its width as determined by radar bathymetry (e.g., Lorenz, 2021; Poggiali et al., 2020), this in itself is not a very specific indicator. There is, however, ample evidence that the coastal geomorphology of Titan's northern seas has been shaped by a variety of processes for example, sea level rise/land sinking (e.g., Planctae Insulae with dendritic shapes, like the islands off the Oman mountains on Earth or the submerged meandering channel of Xanthus Flumen, Lorenz, 2021), some straight coastline segments of Ligeia and rectilinear channels in Trevize Fretum suggestive of tectonic control, and Genova Sinus, the possible tidal flat around Mayda Insula. Confident attribution of the observed morphologies to glacial action would be difficult. In any case, as noted by Lorenz and Lunine (1996) the fact that solid methane can thermodynamically exist is not the same as a large flux of ice accumulation, which is what is needed to drive glacial flow and erosion. Thus we do not claim that the present sea basins were formed by glacial action, only that condensed methane at high latitudes would eventually flow as liquid into these basins.

If Titan's seas were formed by melting of the polar caps, they are likely to have been confined to the polar region. Possible large seas that once extended to low latitudes would require the melting of surface frost to have occurred in epochs with near-global ice sheets a few hundred Myr BP. This appears highly unlikely since a global frost cover maintains a very low surface temperature. The latitudinal profiles of surface temperature and methane frost (Figure 12) in different recent epochs illustrate the situation. Melting of the polar caps is only possible when large portions of the globe are already free of ice so that the low surface albedo and the relatively large atmospheric methane content resulting from the frost ablation jointly act to strongly increase the surface temperature.

For instance, at 20 Myr BP a large fraction of the globe is yet ice-covered (Figure 12b) but the surface temperature is too low (86 K) to melt pure solid methane, even at the equator. At 10 Myr BP the surface temperature at low latitudes reaches the melting point of methane (90.7 K) but no tropical methane frost is left any more, while the ice-covered high latitudes are still too cold to melt the frost. In the present epoch only the polar region is covered by methane deposits. The annual-mean surface temperature exceeds the melting point south of 70°N and the annual maximum surface temperature reaches the melting point even at higher latitudes. This implies that the polar caps may have melted within the past 10 Myr. Without an increase of the solar luminosity, the temperature of the polar cap might have remained slightly below the melting point of methane even in the present epoch. Hence, the increasing solar luminosity may have helped melt the polar caps in the geologically recent past.

Once the polar cap partly melts, liquid methane dissolves atmospheric N<sub>2</sub> with a mole fraction of ~20% (Malaska et al., 2017). Nitrogen dissolution suppresses the freezing point of the hydrocarbon seas (Engle et al., 2021), so that the polar seas could since then be perennially liquid regardless of seasonal temperature variations.

On the other hand, putative tropical paleoseas (Moore & Howard, 2010) are not likely to have been formed by melting of equatorial methane frost deposits considering the model results. The presence of tropical seas may have required a different, warmer climate regime than treated in this study. Choukroun and Sotin (2012) proposed that methane could be steadily emitted from polar methane clathrates because condensed ethane molecules that percolate to the clathrates can substitute the enclathrated methane molecules. Non-zero atmospheric methane content could keep the atmosphere and surface at least warm enough to prevent perennial surface frost. In such a case, massive outgassing may cause extensive rainfall and large methane oceans instead of snowball Titan. Such methane oceans would gradually shrink due to photochemical destruction of methane evaporated from the ocean (Larsson & McKay, 2013). However, it was also pointed out that endorheic tropical lakes could exist even under the present dry climate provided the lakes have no outflow (Tokano, 2020). In either case, previous surface frost is not a necessary condition for the formation of tropical methane seas.

Unless methane outgassing recurs in the near future, the desiccation of the polar seas/lakes should continue in the next few Myr. This would further increase the surface temperature for a while because the greenhouse effect continues to strengthen as a consequence of increasing atmospheric methane content. Once the seas and subsurface methane aquifer are entirely dried up, the atmospheric methane content monotonically decreases and the troposphere gets colder due to weakening greenhouse effect. However, the surface is not likely to get as cold (82 K) as 700 Myr BP because the solar luminosity will be larger in the future.

## 7. Conclusions and Outlook

Paleoclimate simulations were carried out to explore how Titan's climate would respond when large amounts of methane are outgassed after cold epochs of methane depletion. On the one hand, outgassed methane warms the troposphere due to greenhouse effect, but on the other hand it cools down the troposphere if methane snowfall is deposited on the surface and thereby increases the surface albedo. The latter effect becomes predominant when the outgassed methane mass exceeds a certain threshold.

As a consequence of evolving methane outgassing over the past 700 Myr, the model predicts four major steps of climate evolution as illustrated in Figure 13. Outgassed methane initially warms the atmosphere by the greenhouse effect as long as the atmospheric methane content is yet too small for deposition of snowfall. However, when the atmospheric methane content further increases, methane condensation and snowfall set in. Ice sheet formation begins in the cold polar region and gradually extends to low latitudes. Once large portions of the surface are covered by bright snow, the surface and atmospheric temperature fall back due to an ice-albedo feedback. Further methane outgassing increases the depth of the surface frost up to ~100 m, with larger accumulations

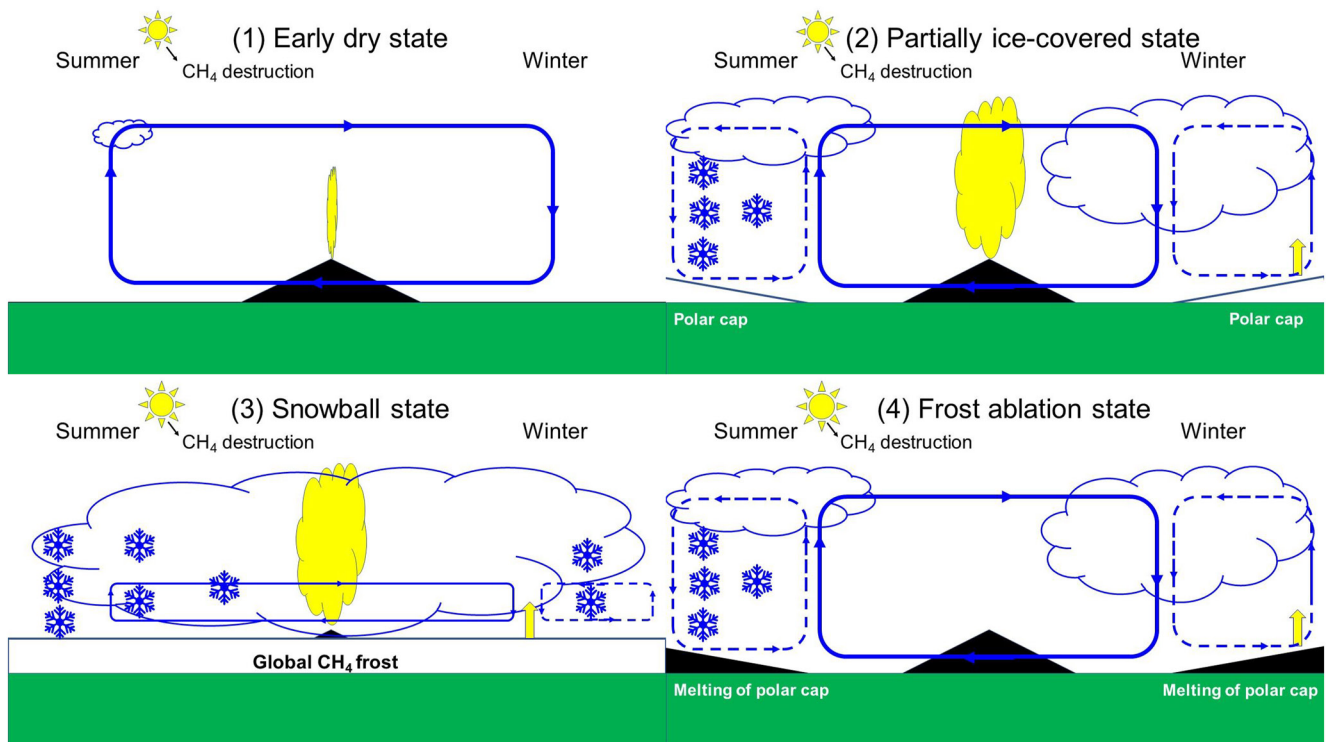


**Figure 13.** Sketch illustrating the four possible major climate states during and after massive methane outgassing into a previously cold  $N_2$  atmosphere predicted by the model. Solid and dashed lines indicate thermally direct and indirect circulation, respectively. The yellow cloud over the mountain indicates the magnitude of methane outgassing. Yellow arrows indicate substantial sublimation.

on elevated terrains where the sublimation rate is smaller and where convergence of moist air often takes place. While the surface frost advances, the climate transitions from a cold methane-depleted state via a warm and relative dry state to a partially ice-covered state and finally to a methane snowball state. After the end of outgassing, frost ablation begins due to photochemical destruction of atmospheric methane. However, it takes several hundred Myr until the surface frost disappears and thereby increases the surface and atmospheric temperature.

The predicted paleoclimate of ice-covered Titan qualitatively differs from the present climate. The partially ice-covered state is characterized by a relatively large meridional temperature gradient across the boundary between frost-covered and frost-free latitudes, seasonally varying snowfall at high latitudes and intense meridional circulation. By contrast, the snowball state is characterized by weak meridional temperature gradients, weak meridional circulation, weak but widespread precipitation and methane saturation down to the surface. The present climate differs from the partially ice-covered state in that the polar caps are liquid and the meridional temperature gradient is small in the absence of polar surface frost.

Among the various input parameters that vary on geological timescales, the methane inventory has the largest impact on the climate evolution. The climate of frost-covered Titan is less sensitive to increasing solar luminosity. This can be contrasted to the climate of Titan with hypothetical liquid hydrocarbon oceans, which dissolve and exsolve atmospheric nitrogen upon surface temperature variations (Lorenz et al., 1999; Lunine & Rizk, 1989; McKay et al., 1993). However, the solar luminosity is more important in epochs that are not fully ice-covered. The albedo of methane frost affects the frost distribution, total frost mass and atmospheric methane content, especially on partially ice-covered Titan. On the other hand, the deceleration of Titan's rotation within the past 1 Gyr has a minor effect on the climate.

It is conceivable that the present polar seas are remnants of past ice sheets. Melting of the polar caps may have occurred within the past tens of Myr when frost retreat as a consequence of photochemical methane destruction increased the greenhouse effect, supported by the increasing solar luminosity.

One of the scientific objectives of the upcoming Dragonfly mission to Titan is to constrain the history of Titan's atmospheric methane (Barnes et al., 2021). It will measure Ar and Ne isotopic distributions to constrain how much outgassing has occurred in Titan's history. In addition, it will also aim to measure or place improved upper limits on the relative Xe, Kr and Ar abundances to test the hypothesis that a significant amount of Titan's volatiles including CH<sub>4</sub> could be trapped in clathrate hydrates. The entirety of these and other measurements by Dragonfly may help understand when and how much methane was outgassed in the past, which is a central assumption of this study.

Lastly, it is important to point out that methane ice sheets can only be expected to have formed over the past 700 Myr if the atmosphere was methane-depleted and therefore cold prior to the onset of the last major outgassing event. If there are some continuous methane sources that can avoid a complete atmospheric methane depletion throughout Titan's history, an entirely different climate evolution without ice sheets might have occurred upon massive methane outgassing.

### Data Availability Statement

The model output used to reproduce the figures in this manuscript is archived at the OSF repository (Tokano, 2021). This repository provides data without restriction or fees.

### Acknowledgments

This work is funded by Deutsche Forschungsgemeinschaft (German Research Foundation, DFG) Grant TO269/5-1. We thank Chris McKay and an anonymous reviewer for helpful comments that helped improve this paper. Open access funding enabled and organized by Projekt DEAL.

### References

- Aharonson, O., Hayes, A. G., Lunine, J. I., Lorenz, R. D., Allison, M. D., & Elachi, C. (2009). An asymmetric distribution of lakes on Titan as a possible consequence of orbital forcing. *Nature Geoscience*, 2, 851–854. <https://doi.org/10.1038/ngeo698>
- Amaral, T., Wake, C. P., Dibb, J. E., Burakowski, E. A., & Stampone, M. (2017). A simple model of snow albedo decay using observations from the Community Collaborative Rain, Hail, and Snow-Albedo (CoCoRaHS-Albedo) Network. *Journal of Glaciology*, 63, 877–887. <https://doi.org/10.1017/jog.2017.54>
- Barnes, J. W., Buratti, B. J., Turtle, E. P., Bow, J., Dalba, P. A., Perry, J., et al. (2013). Precipitation-induced surface brightenings seen on Titan by Cassini VIMS and ISS. *Planetary Science*, 2, 1. <https://doi.org/10.1186/2191-2521-2-1>
- Barnes, J. W., Turtle, E. P., Trainer, M. G., Lorenz, R. D., MacKenzie, S. M., Brinckerhoff, W. B., et al. (2021). Science goals and objectives for the Dragonfly Titan rotorcraft relocatable lander. *The Planetary Science Journal*, 2, 130. <https://doi.org/10.3847/PSJ/abfdcf>
- Bertrand, T., Forget, F., Umurhan, O. M., Moore, J. M., Young, L. A., Protopapa, S., et al. (2019). The CH<sub>4</sub> cycles on Pluto over seasonal and astronomical timescales. *Icarus*, 329, 148–165. <https://doi.org/10.1016/j.icarus.2019.02.007>
- Čadek, O., Kalousová, K., Kvorka, J., & Sotin, C. (2021). The density structure of Titan's outer ice shell. *Icarus*, 364, 114466. <https://doi.org/10.1016/j.icarus.2021.114466>
- Charnay, B., Forget, F., Tobie, G., Sotin, S., & Wordsworth, R. (2014). Titan's past and future: 3D modeling of a pure nitrogen atmosphere and geological implications. *Icarus*, 241, 269–279. <https://doi.org/10.1016/j.icarus.2014.07.009>
- Choukroun, M., & Sotin, C. (2012). Is Titan's shape caused by its meteorology and carbon cycle? *Geophysical Research Letters*, 39, L04201. <https://doi.org/10.1029/2011gl050747>
- Corlies, P., Hayes, A. G., Birch, S. D. P., Lories, R., Stiles, B. W., Kirk, R., et al. (2017). Titan's topography and shape at the end of the Cassini mission. *Geophysical Research Letters*, 44, 11754–11761. <https://doi.org/10.1002/2017GL075518>
- Cornet, T., Cordier, D., Le Bahers, T., Bourgeois, O., Fleurant, C., Le Mouélic, S., & Altobelli, N. (2015). Dissolution on Titan and on Earth: Toward the age of Titan's karstic landscapes. *Journal of Geophysical Research: Planets*, 120, 1044–1074. <https://doi.org/10.1002/2014JE004738>
- Courtin, R., Sim, C. K., Kim, S. J., & Gautier, D. (2012). The abundance of H<sub>2</sub> in Titan's troposphere from the Cassini CIRS investigation. *Planetary and Space Science*, 69, 89–99. <https://doi.org/10.1016/j.pss.2012.03.012>
- de Kok, R., Irwin, P. G. J., & Teanby, N. A. (2010). Far-infrared opacity sources in Titan's troposphere reconsidered. *Icarus*, 209, 854–857. <https://doi.org/10.1016/j.icarus.2010.06.035>
- Doose, L. R., Karkoschka, E., Tomasko, M. G., & Anderson, C. M. (2016). Vertical structure and optical properties of Titan's aerosols from radiance measurements made inside and outside the atmosphere. *Icarus*, 270, 355–375. <https://doi.org/10.1016/j.icarus.2015.09.039>
- Elliot, J. L., Hammel, H. B., Wasserman, L. H., Franz, O. G., McDonald, S. W., Person, M. J., et al. (1998). Global warming on Triton. *Nature*, 393, 765–767. <https://doi.org/10.1038/31651>
- Engle, A. E., Hanley, J., Dustrud, S., Thompson, G., Lindberg, G. E., Grundy, W. M., & Tegler, S. C. (2021). Phase diagram for the methane-ethane system and its implications for Titan's lakes. *The Planetary Science Journal*, 2, 118. <https://doi.org/10.3847/PSJ/abf7d0>
- Ewing, R. C., Hayes, A. G., & Lucas, A. (2015). Sand dune patterns on Titan controlled by long-term climate cycles. *Nature Geoscience*, 8, 15–19. <https://doi.org/10.1038/ngeo2323>
- Fray, N., & Schmitt, B. (2009). Sublimation of ices of astrophysical interest: A bibliographic review. *Planetary and Space Science*, 57, 2053–2080. <https://doi.org/10.1016/j.pss.2009.09.011>
- Fulchignoni, M., Ferri, F., Angrilli, F., Ball, A. J., Bar-Nun, A., Barucci, M. A., et al. (2005). In situ measurements of the physical characteristics of Titan's environment. *Nature*, 438, 785–791. <https://doi.org/10.1038/nature04314>
- Geissler, P. E. (2003). Volcanic activity on Io during the Galileo era. *Annual Review of Earth and Planetary Sciences*, 31, 175–211. <https://doi.org/10.1146/annurev.earth.31.100901.145428>
- Gough, D. O. (1981). Solar interior structure and luminosity variations. *Solar Physics*, 74, 21–34. <https://doi.org/10.1007/BF00151270>
- Graves, S. B. D., McKay, C. P., Griffith, C. A., Ferri, F., & Fulchignoni, M. (2008). Rain and hail can reach the surface of Titan. *Planetary and Space Science*, 56, 346–357. <https://doi.org/10.1016/j.pss.2007.11.001>
- Hansen, C. J., Castillo-Rogez, J., Grundy, W., Hofgartner, J. D., Martin, E. S., Mitchell, K., et al. (2021). Triton: Fascinating moon, likely ocean world, compelling destination! *The Planetary Science Journal*, 2, 137. <https://doi.org/10.3847/PSJ/abffd2>



- Hayes, A. G. (2016). The lakes and seas of Titan. *Annual Review of Earth and Planetary Sciences*, *44*, 57–83. <https://doi.org/10.1146/annurev-earth-060115-012247>
- Hoffman, P. F., Kaufman, A. J., Halverson, G. P., & Schrag, D. P. (1998). A Neoproterozoic snowball Earth. *Science*, *281*, 1342–1346. <https://doi.org/10.1126/science.281.5381.1342>
- Houze, R. A., Jr. (2012). Orographic effects on precipitating clouds. *Reviews of Geophysics*, *50*, RG1001. <https://doi.org/10.1029/2011RG000365>
- Lainey, V., Gomez Casajus, L., Fuller, J., Zannoni, M., Tortora, P., Cooper, N., et al. (2020). Resonance locking in giant planets indicated by the rapid orbital expansion of Titan. *Nature Astronomy*, *4*, 1053–1058. <https://doi.org/10.1038/s41550-020-1120-5>
- Larsson, R., & McKay, C. P. (2013). Timescale for oceans in the past of Titan. *Planetary and Space Science*, *78*, 22–24. <https://doi.org/10.1016/j.pss.2012.12.001>
- Lopes, R. M. C., Kirk, R. L., Mitchell, K. L., Le Gall, A., Barnes, J. W., Hayes, A., et al. (2013). Cryovolcanism on Titan: New results from Cassini RADAR and VIMS. *Journal of Geophysical Research: Planets*, *118*, 416–435. <https://doi.org/10.1002/jgre.20062>
- Lora, J. M., Lunine, J. I., Russell, J. L., & Hayes, A. G. (2014). Simulations of Titan's paleoclimate. *Icarus*, *243*, 264–273. <https://doi.org/10.1016/j.icarus.2014.08.042>
- Lorenz, R. D. (2021). The challenging depth of Titan's seas. *Journal of Geophysical Research: Planets*, *126*, e2020JE006786. <https://doi.org/10.1029/2020JE006786>
- Lorenz, R. D., & Lunine, J. I. (1996). Erosion on Titan: Past and present. *Icarus*, *122*, 79–91. <https://doi.org/10.1006/icar.1996.0110>
- Lorenz, R. D., & Lunine, J. I. (2002). Titan's snowline. *Icarus*, *158*, 557–559. <https://doi.org/10.1006/icar.2002.6880>
- Lorenz, R. D., McKay, C. P., & Lunine, J. I. (1997). Photochemically driven collapse of Titan's atmosphere. *Science*, *275*, 642–644. <https://doi.org/10.1126/science.275.5300.642>
- Lorenz, R. D., McKay, C. P., & Lunine, J. I. (1999). Analytic investigation of climate stability on Titan: Sensitivity to volatile inventory. *Planetary and Space Science*, *47*, 1503–1515. [https://doi.org/10.1016/S0032-0633\(99\)00038-0](https://doi.org/10.1016/S0032-0633(99)00038-0)
- Lorenz, R. D., Wall, S., Radebaugh, J., Boubin, G., Reffett, E., Janssen, M., et al. (2006). The sand seas of Titan: Cassini RADAR observations of longitudinal dunes. *Science*, *312*, 724–727. <https://doi.org/10.1126/science.1123257>
- Lunine, J. I., & Rizk, B. (1989). Thermal evolution of Titan's atmosphere. *Icarus*, *80*, 370–389. [https://doi.org/10.1016/0019-1035\(89\)90147-4](https://doi.org/10.1016/0019-1035(89)90147-4)
- MacKenzie, S. M., Lora, J. M., & Lorenz, R. D. (2019). A thermal inertia map of Titan. *Journal of Geophysical Research: Planets*, *124*, 1728–1742. <https://doi.org/10.1029/2019JE005930>
- Malaska, M. J., Hodyss, R., Lunine, J. I., Hayes, A. G., Hofgartner, J. D., Hollyday, G., & Lorenz, R. D. (2017). Laboratory measurements of nitrogen dissolution in Titan lake fluids. *Icarus*, *289*, 94–105. <https://doi.org/10.1016/j.icarus.2017.01.033>
- McKay, C. P., Pollack, J. B., & Courtin, R. (1989). The thermal structure of Titan's atmosphere. *Icarus*, *80*, 23–53. [https://doi.org/10.1016/0019-1035\(89\)90160-7](https://doi.org/10.1016/0019-1035(89)90160-7)
- McKay, C. P., Pollack, J. B., & Courtin, R. (1991). The greenhouse and anti-greenhouse effects on Titan. *Science*, *253*, 1118–1121. <https://doi.org/10.1126/science.11538492>
- McKay, C. P., Pollack, J. B., Lunine, J. I., & Courtin, R. (1993). Coupled atmosphere-ocean models of Titan's past. *Icarus*, *102*, 88–98. <https://doi.org/10.1006/icar.1993.1034>
- McKay, C. P., Pollack, J. B., Zent, A. P., Cruikshank, D. P., & Courtin, R. (1989). The thermal structure of Triton's atmosphere: Pre-Voyager models. *Geophysical Research Letters*, *16*, 973–976. <https://doi.org/10.1029/GL016i008p00973>
- Mitri, G., Lunine, J. I., Mastrogiuseppe, M., & Poggiali, V. (2019). Possible explosion crater origin of small lake basins with raised rims on Titan. *Nature Geoscience*, *12*, 791–796. <https://doi.org/10.1038/s41561-019-0429-0>
- Moore, J. M., & Howard, A. D. (2010). Are the basins of Titan's Hotei Regio and Tui Regio sites of former low latitude seas? *Geophysical Research Letters*, *37*, L22205. <https://doi.org/10.1029/2010GL045234>
- Niemann, H. B., Atreya, S. K., Bauer, S. J., Carignan, G. R., Demick, J. E., Frost, R. L., et al. (2005). The abundances of constituents of Titan's atmosphere from the GCMs instrument on the Huygens probe. *Nature*, *438*, 779–784. <https://doi.org/10.1038/nature04122>
- Niemann, H. B., Atreya, S. K., Demick, J. E., Gautier, D., Haberman, J. A., Harpold, D. N., et al. (2010). Composition of Titan's lower atmosphere and simple surface volatiles as measured by the Cassini-Huygens probe gas chromatograph mass spectrometer experiment. *Journal of Geophysical Research*, *115*, E12006. <https://doi.org/10.1029/2010JE003659>
- Nimmo, F., & Bills, B. G. (2010). Shell thickness variations and the long-wavelength topography of Titan. *Icarus*, *208*, 896–904. <https://doi.org/10.1016/j.icarus.2010.02.020>
- Pierrehumbert, R., Abbott, S., Voigt, A., & Koll, D. (2011). Climate of the Neoproterozoic. *Annual Review of Earth and Planetary Sciences*, *39*, 417–460. <https://doi.org/10.1146/annurev-earth-040809-152447>
- Poggiali, V., Hayes, A. G., Mastrogiuseppe, M., Le Gall, A., Lalich, D., Gómez-Leal, I., & Lunine, J. I. (2020). The bathymetry of Moray Sinus at Titan's Kraken Mare. *Journal of Geophysical Research: Planets*, *125*, e06558. <https://doi.org/10.1029/2020JE006558>
- Saillenfest, M., Lari, G., & Boué, G. (2021). The large obliquity of Saturn explained by the fast migration of Titan. *Nature Astronomy*, *5*, 345–349. <https://doi.org/10.1038/s41550-020-01284-x>
- Suarez, M. J., & Takacs, L. L. (1995). *Documentation of the ARIES/GEOS dynamical core: Version 2* (Vol. 5). NASA Tech. Memorandum 104606.
- Tobie, G., Lunine, J. I., & Sotin, C. (2006). Episodic outgassing as the origin of atmospheric methane on Titan. *Nature*, *440*, 61–64. <https://doi.org/10.1038/nature04497>
- Tokano, T. (2005). Meteorological assessment of the surface temperatures on Titan: Constraints on the surface type. *Icarus*, *173*, 222–242. <https://doi.org/10.1016/j.icarus.2004.08.019>
- Tokano, T. (2009). Impact of seas/lakes on polar meteorology of Titan: Simulation by a coupled GCM-sea model. *Icarus*, *204*, 619–636. <https://doi.org/10.1016/j.icarus.2009.07.032>
- Tokano, T. (2017). Nitrogen condensation in Titan's atmosphere under contemporary atmospheric composition. *Icarus*, *289*, 120–133. <https://doi.org/10.1016/j.icarus.2017.02.005>
- Tokano, T. (2019). Orbitally and geographically caused seasonal asymmetry in Titan's tropospheric climate and its implication for the lake distribution. *Icarus*, *317*, 337–353. <https://doi.org/10.1016/j.icarus.2018.07.025>
- Tokano, T. (2020). Stable existence of tropical endorheic lakes on Titan. *Geophysical Research Letters*, *47*, e2019GL086166. <https://doi.org/10.1029/2019GL086166>
- Tokano, T. (2021). 2021JE007081. OSF repository. <https://doi.org/10.17605/osf.io/yrj5h>
- Tokano, T., McKay, C. P., Neubauer, F. M., Areya, S. K., Ferri, F., Fulchignoni, M., & Niemann, H. B. (2006). Methane drizzle on Titan. *Nature*, *442*, 432–435. <https://doi.org/10.1038/nature04948>
- Tokano, T., Neubauer, F. M., Laube, M., & McKay, C. P. (1999). Seasonal variation of Titan's atmospheric structure simulated by a general circulation model. *Planetary and Space Science*, *47*, 493–520. [https://doi.org/10.1016/S0032-0633\(99\)00011-2](https://doi.org/10.1016/S0032-0633(99)00011-2)

- Tokano, T., Neubauer, F. M., Laube, M., & McKay, C. P. (2001). Three-dimensional modeling of the tropospheric methane cycle on Titan. *Icarus*, 153, 130–147. <https://doi.org/10.1006/icar.2001.6659>
- Tomasko, M. G., Bézard, B., Doose, L., Engel, S., Karkoschka, E., & Vinatier, S. (2008). Heat balance in Titan's atmosphere. *Planetary and Space Science*, 56, 648–659. <https://doi.org/10.1016/j.pss.2007.10.012>
- Turtle, E. P., Perry, J. E., Barbara, J. M., Del Genio, A. D., Rodriguez, S., Le Mouélic, S., et al. (2018). Titan's meteorology over the Cassini mission: Evidence for extensive subsurface methane reservoirs. *Geophysical Research Letters*, 45, 5320–5328. <https://doi.org/10.1029/2018GL078170>
- Westlake, J. H., Waite, J. H., Bell, J. M., & Perryman, R. (2014). Observed decline in Titan's thermospheric methane due to solar cycle drivers. *Journal of Geophysical Research: Space Physics*, 119, 8586–8599. <https://doi.org/10.1002/2014JA020394>
- Wilson, E. H., & Atreya, S. K. (2004). Current state of modeling the photochemistry of Titan's mutually dependent atmosphere and ionosphere. *Journal of Geophysical Research*, 109, E06002. <https://doi.org/10.1029/2003JE002181>
- Wong, M. L., Yung, Y. L., & Gladstone, G. R. (2015). Pluto's implications for a snowball Titan. *Icarus*, 246, 192–196. <https://doi.org/10.1016/j.icarus.2014.05.019>
- Yung, Y. L., Allen, M., & Pinto, J. P. (1984). Photochemistry of the atmosphere of Titan: Comparison between model and observations. *The Astrophysical Journal - Supplement Series*, 55, 465–506. <https://doi.org/10.1086/190963>